Title
Discrete Element Modeling of Impact Damage on Thermal Barrier Coatings

Author
Minor, Peter Michel

Publication Date
2013

Discrete Element Modeling of Impact Damage on Thermal Barrier Coatings

by

Peter Michel Minor

A dissertation submitted in partial satisfaction of the
requirements for the degree of
Doctor of Philosophy

in

Engineering - Mechanical Engineering

in the

Graduate Division

of the

University of California, Berkeley

Committee in charge:

Professor Tarek I. Zohdi, Co-chair
Professor Paul K. Wright, Co-chair
Professor James W. Evans
Professor David A. Dornfeld

Fall 2013

Discrete Element Modeling of Impact Damage on Thermal Barrier Coatings

Abstract

Discrete Element Modeling of Impact Damage on Thermal Barrier Coatings

by

Peter Michel Minor

Doctor of Philosophy in Engineering - Mechanical Engineering

University of California, Berkeley

Professor Tarek I. Zohdi, Co-chair

Professor Paul K. Wright, Co-chair

Natural gas turbines have become an increasingly important part of the energy landscape in the United States, currently accounting for 19% of all electricity production. Efforts to increase thermal efficiency in gas turbines has led to the adoption of highly porous ceramic thermal barrier coatings (TBCs), which are susceptible to erosion and foreign object impact damage. Despite significant investment to improve the design of TBCs, few numerical tools exist which are capable of both accurately capturing the specific failure mechanisms inherent to TBCs and iterating design parameters without the requirement for coupled experimental data.

To overcome these limitations, a discrete element model (DEM) was created to simulate the microstructure of a TBC using a large-scale assembly of bonded particles. Acting as Lagrangian nodes, the particles can be combined to create accurate representations of TBC geometry and porosity. The inclusion of collision-driven particle dynamics and bonds derived from displacement-dependent force functions endow the microstructure model with the ability to deform and reproduce damage in a highly physical manner. Typical TBC damage mechanisms such as compaction, fracture and spallation occur automatically, without having to tune the model based on experimental observation. Therefore, the first order performance of novel TBC designs and materials can be determined numerically, greatly decreasing the cost of development.

To verify the utility and effectiveness of the proposed damage model framework, a nanoindentation materials test simulation was developed to serve as a test case. By varying model parameters, such as the porosity of the TBC and maximum applied indenter force, nanoindentation data from more than one hundred distinct permutations was gathered and analyzed. This data was used to calculate the elastic modulus (E) and hardness (H) of the simulated microstructure, which could then be compared to known experimental material property values. A good correlation was found between the predicted properties calculated by the model and those found through experimental nanoindentation tests. Furthermore, conforming to the benefits of DEM, the model was able to accurately recreate the same ma-

terial damage characteristics observed in literature, such as the onset of inelastic deformation from fracture.

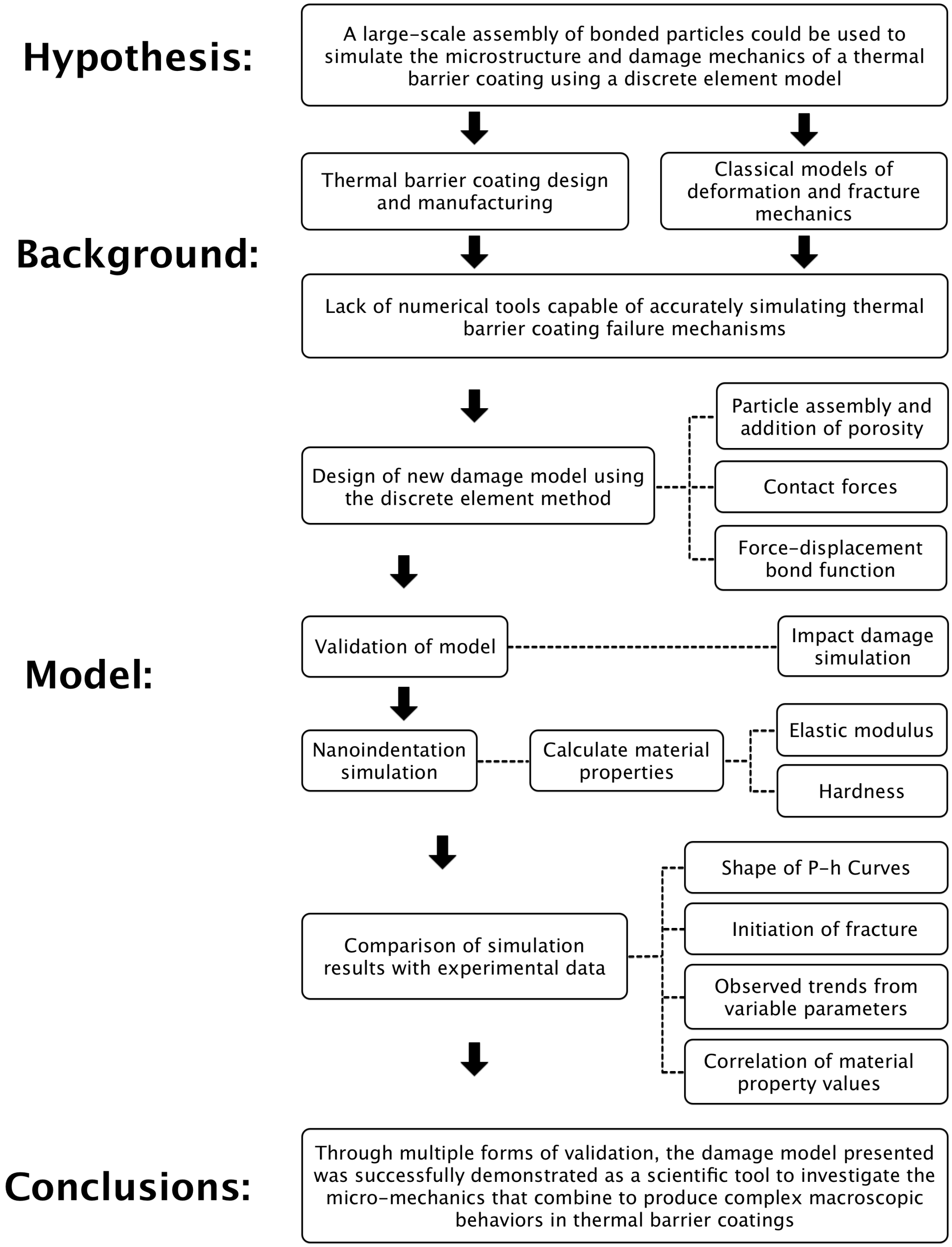

Dedicated to science.

Because science.

Contents

List of Figures

List of Tables

Acknowledgments

I would like to express my deep appreciation for both my advisers, Professor Paul Wright and Professor Tarek Zohdi. Paul has been my mentor since I was an undergraduate student, and inspired me to pursue my graduate education. He always took the time necessary to ensure my happiness and productivity, even when his schedule did not allow for it. Tarek motivated me to learn new skills and improve my abilities as an engineer. His expertise and gentle encouragement helped me navigate through the moments when research challenges felt insurmountable. Without the support and guidance I received from both advisers, I would never have been able to make it this far. You've both helped me become the person I am today.

I would also like to acknowledge the other members of my dissertation committee, Professor James Evans and Professor David Dornfeld. Jim, I appreciate your willingness to provide materials science guidance when needed. My research was undoubtedly improved by your influence. Professor Dornfeld, thank you for agreeing to serve on my committee on such short notice.

Thank you to all my friends and colleagues in the BMI and CMRL labs. The laughter and discussions we shared brought me back to lab each day. I have learned more during casual conversations with my lab friends than from any of the classes I took.

I am grateful for the support provided to my research project by Siemens Energy. They took a chance on a couple of students. I hope we were able to prove our worth.

My family deserves to share in my accomplishment, as they have been instrumental to my development. My intelligence, work ethic, passion for knowledge and difficult temperament can all be attributed to the influence of my parents. My siblings have always been a limitless source of adventure, inspiration, and annoyance.

Finally, I want to thank Charlotte for her unrelenting support and love. She pushes me forward, especially when I am too wearied or scared to make progress on my own. The time we have spent together has made me a better person, in every way possible.

Chapter 1

Introduction and Problem Statement

1.1 Introduction to Gas Turbines

Natural gas turbines are an increasingly important contributor to the global energy landscape. Due to their cost effectiveness and relative cleanliness, gas turbines now account for 19% of electricity production in the US, for a total of 987 billion kWh every year [28].

As with all heat engines, gas turbines generate electricity by converting thermal energy into mechanical work. Compressed air is fed into a combustor, where it is mixed with natural gas and ignited. The resulting high-temperature and high-velocity gases are injected through several rows of turbine blades, causing the turbine shaft to spin. The rotating shaft is connected to an electric generator, converting mechanical energy into electric energy. A diagram outlining the different stages of a gas turbine is shown in Figure 1.1.

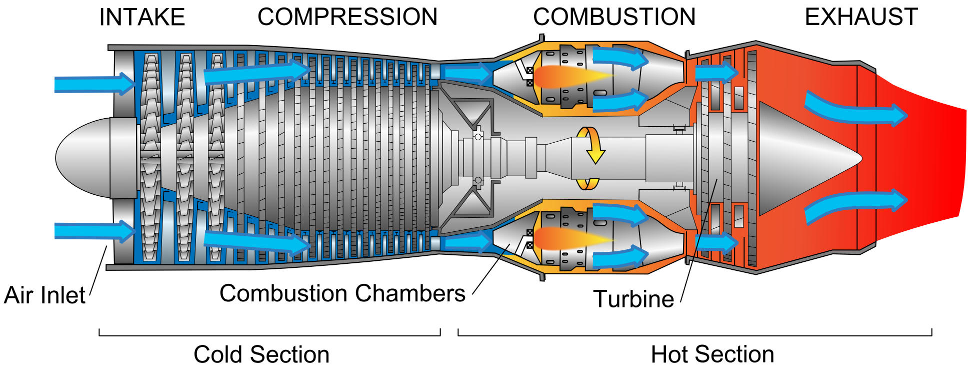

Figure 1.1: Simplified diagram of a gas turbine, illustrating the different operational stages. Damage from foreign object impacts are most problematic in the ‘hot section’, where high temperature combustion gases are injected through rows of turbine blades [1].

True of any heat engines, the maximum efficiency of gas turbines is described by the Carnot efficiency in Equation 1.1.

$$\eta_{max} = 1 - \frac{T_c}{T_h} \tag{1.1}$$

As seen in Equation 1.1, one of the simplest methods for improving the efficiency of a gas turbine is by raising the output temperature from the combustor. Accordingly, manufacturers have adopted new technologies which have allowed operating temperatures to increase by more than 60% over the last five decades [50]. Modern turbines operate at temperatures up to 1400°C, which is more than 100°C above the melting point of the metal substructure.

1.2 Motivation

The bulk of the efficiency improvements can be credited to the introduction of thermal barrier coatings. Due to their extremely low thermal conductivity, these coatings are able to lower the temperature experienced by turbine components, allowing for a higher maximum operating temperature. The primary mechanism for reducing the conductivity of thermal barrier coatings is through the addition of porosity. More advanced coating systems can be designed with more than 30% porosity, by volume.

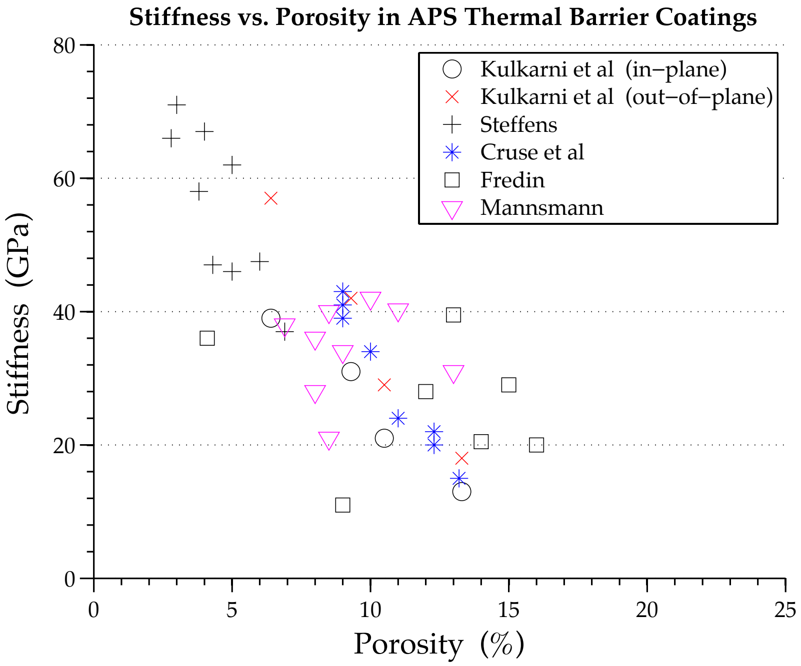

Figure 1.2: Relationship between the stiffness of air plasma sprayed thermal barrier coatings and porosity, added as a percentage of volume [23, 43].

The drive towards greater thermal efficiency has also led to reduced structural strength. As can be seen in Figure 1.2, increasing the porosity tends to reduce the stiffness of thermal barrier coatings. This trend leaves gas turbines more susceptible to impact damage from various foreign objects, such as particulates. Multiple impacts can lead to significant removal of the coating, putting the turbine at risk.

1.3 Statement of Purpose

With modern high performance computing capabilities, an opportunity exists to utilize numerical analysis to inform the design of new thermal barrier coating architectures and materials that do not exhibit the trade-off shown in Figure 1.2. Unfortunately, most impact damage models to date have used continuum mechanics to describe the material dynamics, even though they are ill-suited for the task of simulating highly porous ceramics. Treating thermal barrier coatings like a homogeneous solid ignores the microstructure that provides its low conductivity characteristics. In the same manner, the microstructure is also what defines crack propagation and the extent of inelastic deformation. Therefore, in order to continue contributing to the vision of higher gas turbine efficiency in the future, a better understanding of thermal barrier coating durability and failure will be required.

To address this need, the aim of this dissertation is to develop a damage model that more accurately reflects the mechanical behavior of thermal barrier coatings. This can be done by utilizing the discrete element method to numerically define the microstructure. Thus, the coatings will be modeled using arrays of bonded particles, which include the pores and cracks found in the actual materials. By mimicking a more authentic coating structure, it will be possible to recreate an accurate physical representation of impact damage. Once developed, the damage model will be validated using nanoindentation, which is a standard materials test often applied to thermal barrier coatings. If the nanoindentation simulation is able to match the damage characteristics and material properties found in experimental nanoindentation tests, it would suggest that the model is able to successfully capture the mechanical behavior of thermal barrier coatings.

Chapter 2

Thermal Barrier Coatings

2.1 System of Materials

Thermal barrier coatings (TBC) are an advanced material system, comprised of multiple functional layers working in parallel to create a durable barrier to high temperature gases. They're applied to hot sections of gas turbines, most notably the blades. Thermal barrier coatings have a very low thermal conductivity, which reduces the temperature experienced by the turbine components significantly. This extends the life of the components, creates a safer operating environment, and maximizes thermal efficiency.

Thermal barrier coatings typically consist of four distinct layers: a superalloy substrate, a metallic bond coat, a thermally-grown oxide, and a ceramic top coat. The main role of the superalloy is to provide structural strength and high-temperature creep resistance. A bond coat is used to help correct the thermal expansion mismatch between the superalloy and ceramic layer. Thermally-grown oxides slow the process of oxidation. And finally, the ceramic topcoat is the main temperature resistant component, protecting the structure from extreme temperature environments.

2.2 Coating Design

2.2.1 Nickel-Based Superalloy

Due to its high temperature strength and resistance to inelastic deformation, nickel-based superalloys are widely used for structural components of high temperature turbine sections. A gas turbine blade constructed of single crystal nickel-based superalloy is shown in Figure 2.2. No other commercially available alloy provides a more suitable combination of stiffness, high-temperature creep resistance, and protection from oxidation and fatigue. These properties do not begin to degrade until 850°C, and nickel-based superalloys can survive temperatures as high as 1200°C for a short time [32].

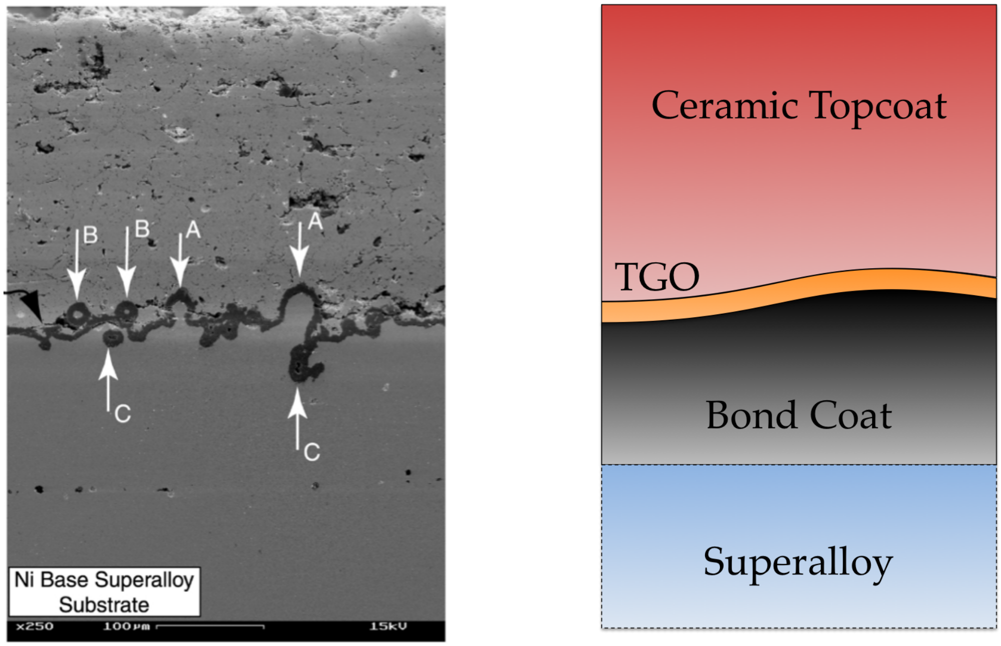

Figure 2.1: Experimental and illustrated images showing the different material layers that constitute a thermal barrier coating system [12].

Figure 2.2: Gas turbine blade constructed of single-crystalline Ni-based superalloy [45].

Some turbine components are fabricated using fully crystalline superalloys because grain boundaries are sites for damage accumulation at high temperatures. Removing the grain boundaries also reduces creep, eliminating a primary mechanism for inelastic deformation.

Table 2.1: Typical properties of nickel-based superalloys [32].

Property	**Typical Values**
Density:	7.7 – 9.0 g/cm^3
Melting Temperature:	1320 – 1450°C
Elastic Modulus:	Room temp: 210 GPa
	800°C: 160 GPa
Thermal Expansion:	$8 - 18 \times 10^{-6}$/°C
Thermal Conductivity:	Room temp: 11 W/m-K
	800°C: 22 W/m-K

2.2.2 Metallic bond coat (NiCrAlY)

For durability reasons, the ceramic top coat cannot be applied directly onto the superalloy turbine structure. Significant differences in composition prevent the two materials from forming a sufficiently robust linkage to counteract delamination. Therefore, an intermediate layer is added that contains elements of both materials, creating bonding sites on both sides. This layer is deposited on top of the superalloy, and is called the metallic bond coat.

Air plasma sprayed coatings typically employ a MCrAlY bond coat, where the M can stand for any number of metals. But since nickel is the primary functional element of the base metal, a NiCrAlY formulation would be used to promote chemical bonding with the superalloy. NiCrAlY coatings also contain up to 1 wt% yttria to enhance adherence to the topcoat, which is composed on yttria-stabilized zirconia. Finally, the bond coat is ductile at high temperatures and has a coefficient of thermal expansion in-between the topcoat and superalloy, helping to mitigate the formation of stresses at the interface rising from thermal expansion mismatch between the two layers.

Table 2.2: Typical properties of NiCrAlY bond coats [33].

Property	**Typical Values**
Density:	8.0 g/cm^3
Elastic Modulus:	Room temp: 140 – 230 GPa
	1000°C: 60 – 130 GPa
Thermal Expansion:	$13 - 16 \times 10^{-6}$/°C

2.2.3 Thermally Grown Oxide (TGO)

Even though nickel-based superalloys are already resistant to corrosion, prolonged exposure to hot gases necessitates additional protection. Hence, a thin layer of encapsulation called the thermally grown oxide is formed from the metal bond coat to further insulate the superalloy from the harsh environment. High aluminum content in the NiCrAlY bond coat leads to the formation of a stable Al_2O_3 oxide on the surface exposed to oxygen. This alumina layer prevents further oxidation of the bond coat, and consequently, also protects the superalloy.

2.2.4 Ceramic Top Coat

The ceramic topcoat is the main temperature resistant component of the thermal barrier coating system. The most commonly utilized top coat material is yttria-stabilized zirconia (YSZ), due to its low thermal conductivity and superior mechanical properties. Additionally, compared to other choices of thermal barrier coating materials shown in Figure 2.3, the thermal conductivity of yttria-stabilized zirconia remains low over a wider temperature range. Beyond conductivity, yttria-stabilized zirconia also has a high thermal expansion coefficient, which better matches with values of the underlying layers.

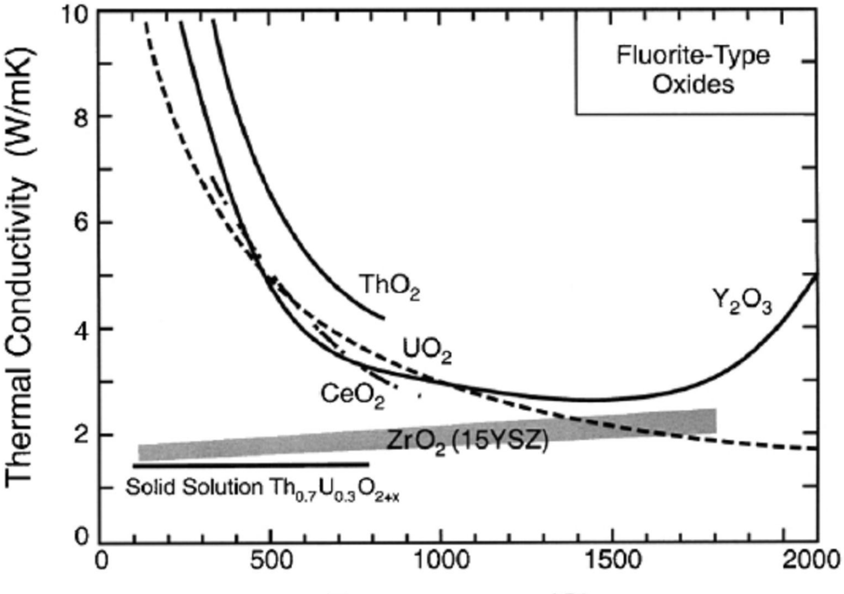

Figure 2.3: Thermal conductivity of yttria-stabilized zirconia, compared to other potential thermal barrier coating materials, as a function of operating temperature of the gas turbine [33].

Zirconia is stabilized with yttria in order to keep the material in a cubic phase. As shown by the diagram in Figure 2.4, cooling zirconia without any additives will cause a transition from a tetragonal to a fully monoclinic phase. This can be problematic because the conversion to the monoclinic phase activates a significant volume expansion, on the order of 4-6% [11]. Since thermal expansion mismatch between layers is already an area of concern, repeated thermal cycles could cause the thermal barrier coating to fatigue. By adding a small percentage of yttria (Y_2O_3), the phase becomes partially stabilized and the volume change is reduced. An addition of 3-10% by weight is common for yttria-stabilized zirconia in thermal barrier coatings.

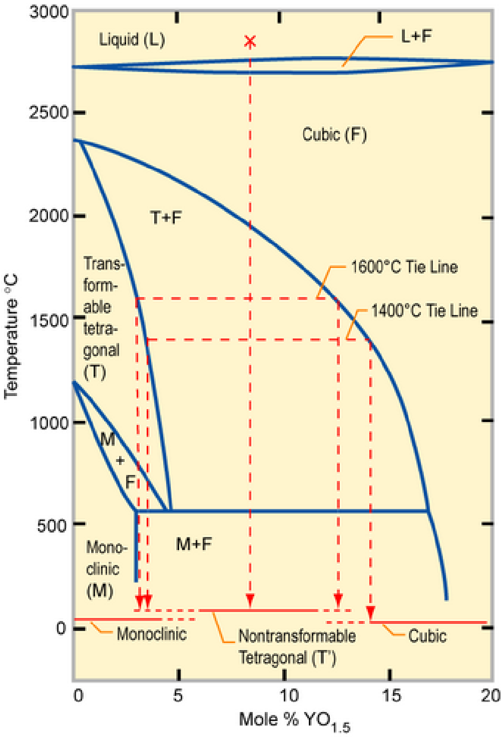

Figure 2.4: Phase diagram for yttria-stabilized zirconia, varying the volume fraction of yttria. The addition of yttria is intended to weaken the transition from cubic to monoclinic phase [40].

On its own, bulk yttria-stabilized zirconia has a thermal conductivity in the range of 2.0 W/m-K, which is lower than stainless steel by a factor of ten. To reduce the thermal conductivity even further, the ceramic topcoat can be produced with up to 35% porosity. Since air has a thermal conductivity of 0.02 W/m-K, the overall conductivity of the porous coating layer is reduced by more than half.

Table 2.3: Typical properties of a yttria-stabilized zirconia topcoat [32].

Property	**Typical Values**
Density (bulk):	6.05 g/cm^3
Thickness:	$200 - 500$ μm
Porosity:	$5 - 35\%$ by vol
Elastic Modulus (bulk):	$25 - 150$ GPa
Thermal Expansion:	$10 - 12 \times 10^{-6}$ 1/K
Thermal Conductivity (bulk):	0.8 W/m-K

2.2.5 Manufacturing Techniques

The most common method for depositing yttria-stabilized zirconia is by air plasma spraying (APS). Other techniques are sometimes used as well, such as electron beam physical vapor deposition (EB-PVD). However, they are typically reserved for specific applications, since air plasma sprayed coatings can be made with a lower thermal conductivity and are more economical to produce.

2.2.5.1 Air Plasma Spray

The characteristically low thermal conductivity of coatings produced by this technique is a consequence of how materials are deposited. As portrayed in Figure 2.5, air plasma spraying operates by injecting a powder material into a hot plasma jet. The powder is quickly heated to a temperature approaching 10,000K, resulting in a stream of molten droplets flying towards the substrate. Upon impact, the droplets are flattened into a pancake-like splat, measuring 1-10 microns in thickness and 200-400 microns in diameter. Coatings are built up to the desired thickness by layering these splats on top of each other.

The end result is a coating with the lamellar morphology shown in Figure 2.6. The splats land on the substrate in a random pattern and immediately solidify on contact. The lack of resolidification among neighboring splats leaves a network of inter-splat boundaries, pores and cracks between individual splats. The ubiquitous and arbitrary nature of these voids provides an ideal form of insulation, as the number of unbroken heat conduction paths through the coating thickness is diminished. To magnify this effect, the air plasma spray parameters can be optimized to provide a user-defined volume fraction of porosity, which can be as high as 35% for advanced thermal barrier coatings.

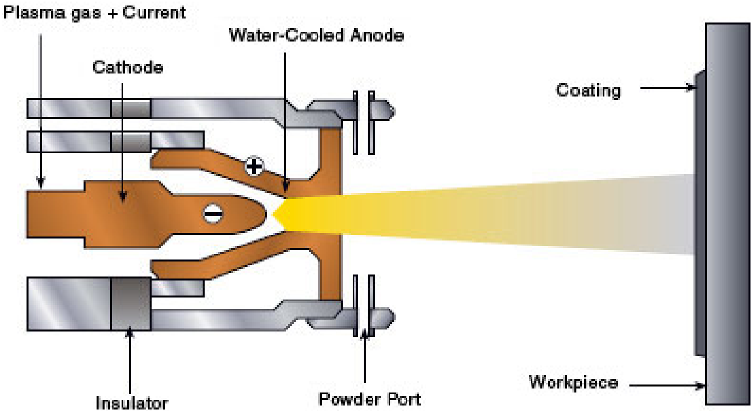

Figure 2.5: Illustration of the air plasma spray process, showing relevant components [10].

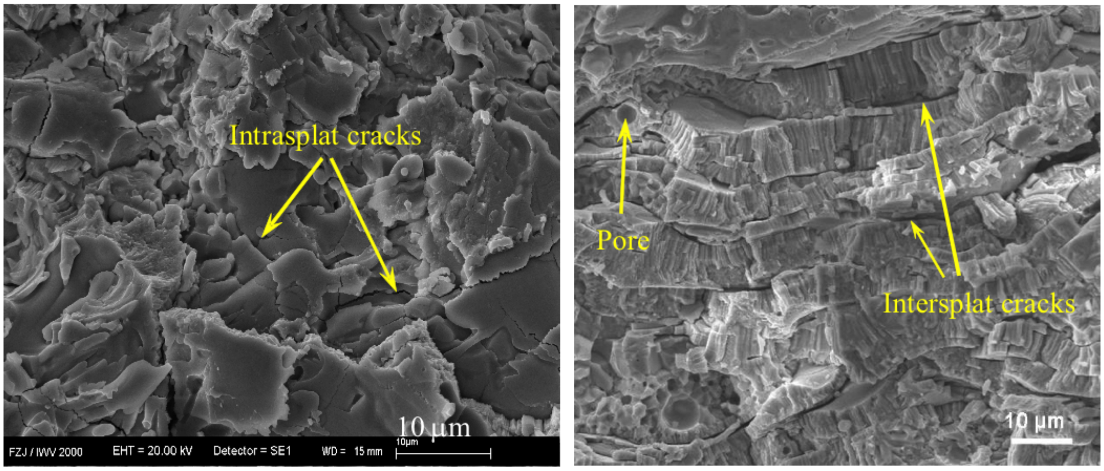

Figure 2.6: Thermal barrier coating morphology produced by air plasma spraying. The left image a top view of the coating, and the right is a view from the side. [33].

2.3 Failure mechanisms

As mentioned in Section 1.1, the reliability of thermal barrier coatings is critical to the survival of gas turbines, as operating temperatures are routinely above the yield point of the superalloy structure. Any type of damage leading to significant removal of the coating can put the turbine at risk. The odds of this happening are non-trivial, as the interior section of a gas turbine is an extremely harsh environment. Thermal barrier coatings must be able to withstand numerous types of physical attack, including high energy impact, erosion, thermal fatigue, residual stress buildup between layers, oxidation and chemical corrosion. The mechanisms of each damage response, and the numerical methods required to model them, are all highly specific. Therefore, this work will focus on the effects of high energy impact, although many of the principles will apply to erosion as well.

2.3.1 Impact by Foreign Objects

Impact damage occurs when foreign objects are introduced into the flow stream of a gas turbine, and come into contact with one of the many components shielded by thermal barrier coatings. Fitting with their name, the precise origin and composition of these foreign objects are not well understood. They are believed to be constructed of either ceramic or metal, and take on a variety of shapes, including spherical, cylindrical and cubic. The critical dimension (i.e. diameter in a sphere) can be as large as half an inch. Impact velocity is thought to vary significantly, up to a maximum of 175 m/s.

2.3.2 Impact Damage

Upon impact, a foreign object exerts a great amount of stress on the thermal barrier coating microstructure. The subsequent damage can manifest itself in diverse forms. In all cases, the foreign object will penetrate the surface, leaving a crater at the impact site. The region surrounding the crater will undergo inelastic deformation, often manifested as compaction in regions with high porosity. The propagation of stress waves from the impact will also cause fracture damage, with crack surfaces expanding into the coating. The extent of the fracture damage will depend heavily on the microstructure of the thermal barrier coating. However, if cracking is extensive enough to cause several cracks to coalesce across a section of the coating, large pieces of material can be ejected in a process called spallation. Figure 2.7 displays a turbine blade where much of the thermal barrier coating has been removed due to repeated spallation.

As was the case with thermal conductivity, the morphology of thermal barrier coatings is a critical component to the damage processes caused by impact. The pathways for fracture and deformation will inevitably be defined by the microstructure shown previously in Figure 2.6. Cracks will more readily propagate through weak splat interfaces, where fewer material bonds exist to impede its progression. Thus, one coating sample could conceivably be more liable to spall than another sample with an equal amount of porosity, if its microstructural arrangement happens to have a greater concentration of contiguous crack surfaces. More generally, differences in the microstructure alone are sufficient to cause a measurable change in the material damage response, and as a consequence, the material properties too.

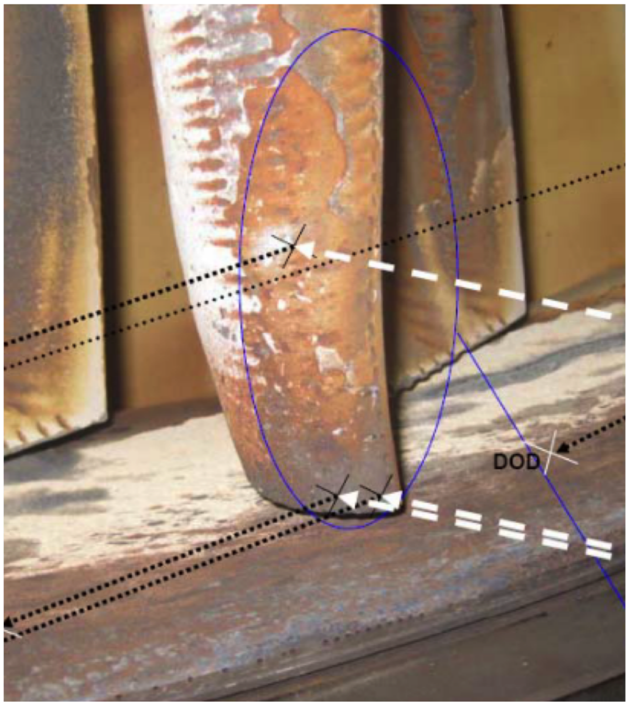

Figure 2.7: Gas turbine blade showing significant removal of its thermal barrier coating due to foreign object impact damage [44]

Chapter 3

Review of Numerical Methods

3.1 Classical Models of Elastic Deformation and Fracture Mechanics

While much of classical mechanics does not apply directly to thermal barrier coatings, an understanding of the theoretical basis on which it is derived is of paramount importance. Any newly proposed damage model must be rooted in the same physical principles, such as thermodynamic equilibrium, in order to produce meaningful results. Therefore, this section will include a select treatment of classical models of deformation and fracture, for the purpose of discussing both the shortcomings of the current form with respect to impact damage on thermal barrier coatings, and drawing inspiration for ways to make improvements.

3.1.1 Von Mises Yield Criterion

The von Mises yield criterion is a common method for determining the onset of yielding in a material subject to external stresses. It can be used to determine the size of the yield zone in front of a crack, as shown in Figure 3.1, which is indicative of potential crack elongation. It can also be used to estimate the amount of total deformation caused by an external load, such as an impact.

The von Mises criterion is based on the accumulation of strain energy, often measured as a density, since it tends to occur in a localized region. When a material is subject to an external force, work is done to cause the deformation that follows. Strain energy density is the potential energy per unit volume that is stored in the form of deformation. In the case of elastic deformation, the total strain energy will be fully recovered when the force is removed from the body. The strain energy density can be decomposed into two components: dilatational strain energy density is due to change in volume, and distortional strain energy density is responsible for change in shape.

According to the von Mises criterion, a material will begin to yield when its distortional energy density passes a critical value. Thus, the distortional energy can be expressed as a

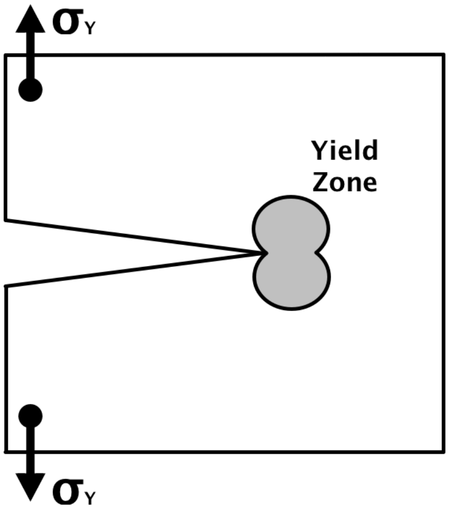

Figure 3.1: Yield zone developed on a plate due to von Mises stresses at the tip of a crack, length c. The onset of yield is caused by the application of an external yield stress σ_Y

function of the von Mises stress, which is derived using the relationship for critical stress in a uniaxial tensile test. The product is the von Mises yield criterion shown in Equation 3.1.

$$\sigma_Y^2 = \frac{1}{2}\left[(\sigma_{11}-\sigma_{22})^2 + (\sigma_{22}-\sigma_{33})^2 + (\sigma_{33}-\sigma_{11})^2 + 6\left(\sigma_{23}^2+\sigma_{31}^2+\sigma_{12}^2\right)\right] \tag{3.1}$$

From this equation, σ_Y is the applied yield stress, $\sigma_{11}, \sigma_{22}, \sigma_{33}$ are the normal stresses in the 1,2,3 directions acting at the crack tip, and $\sigma_{12}, \sigma_{23}, \sigma_{31}$ are the shear stresses acting at the crack tip.

Since von Mises assumes failure due to distortional energy, it only holds when considering ductile materials, such as metals. It is not an accurate failure criterion for brittle ceramics. However, when dealing with ductile materials, the von Mises yield criterion can be applied successfully to calculate the deformation due to impact [4].

3.1.2 Inglis Equation

Some of the early treatments of fracture mechanics were the Inglis equations [19], which provided insight into the microstructural mechanics of crack propagation. It was the first analysis to show that the local stress at a sharp crack tip was many times greater than the externally applied stress, effectively being concentrated by the crack geometry. Furthermore, in contrast to the assumption of an infinitely sharp crack tip by von Mises, Inglis approximated the crack as a narrow ellipse. With this simple modification, the specific local stress could be numerically defined as a function of the crack dimensions.

To illustrate this result, Figure 3.2 shows a plate with an elliptical crack of length c and a crack tip with radius of curvature equal to ρ. An external stress σ_a is applied to the plate.

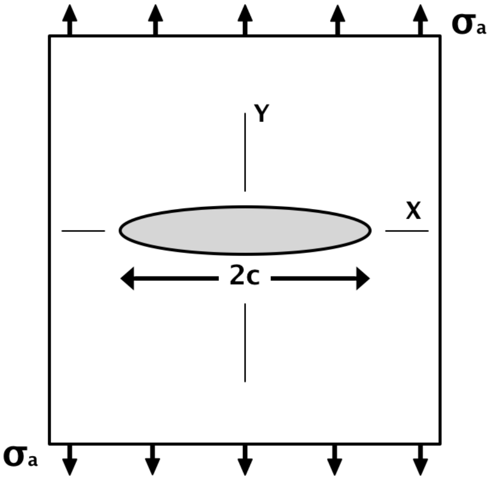

Figure 3.2: Elliptical crack contained by a two-dimensional plate, with length $2c$ and a radius of curvature at the crack tip equal to ρ. An external stress σ_a is applied to the boundary.

If the dimensions of the crack are assumed to be small compared to the plate and Hooke's Law is valid everywhere, linear elasticity theory can be used to derive Equation 3.2, relating the stress at the crack tip σ_c to the external stress σ_a.

$$\frac{\sigma_c}{\sigma_a} = 2\left(\frac{c}{\rho}\right)^{\frac{1}{2}} \tag{3.2}$$

From this, we see that if the crack tip is small compared the the length of the crack, the stress at the crack tip can be magnified by several orders of magnitude. This is also an important result because the stress at the crack tip can be related to the stress required for crack extension. As shown in the next section, it is then possible to establish a criterion for the applied stress which will cause the onset of fracture.

3.1.3 Griffith Theory

Most materials tend to experience fracture damage when stressed beyond a critical point. Griffith was able to rationalize this concept by connecting it back to a critical fracture stress, which activates the extension of a preexisting flaw. To accomplish this, he considered the thermodynamics of crack propagation.

Using Figure 3.3 as an example, Griffith theory suggests that cracks exist in a state of thermodynamic equilibrium. Energy is split into a mechanical component, which includes the bonds holding a material together and any external stresses leading to crack growth, and a surface component, which is free energy consumed by new damage surfaces created by crack growth. Assuming the crack acts reversibly, the sum of these energies is conserved.

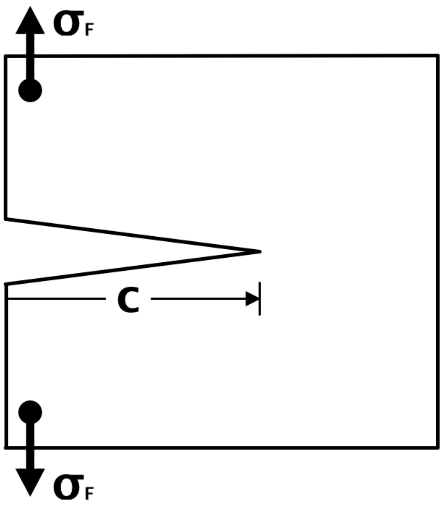

Figure 3.3: Opening of crack surface of length c due to the application of a critical failure stress σ_F

When a crack is extended, due to rupture of the material bonds, mechanical energy is converted to surface energy. This conversion manifests itself physically with a reduction in the number of remaining bonds and a larger crack surface. Returning to the example of a cracked plate constructed of some known material, it is possible to relate the bonding component of the mechanical energy to the plate's elastic modulus E, the external potential acting on the plate to a critical failure stress σ_F, and the surface component to the surface energy γ of the plate material. The end result is Equation 3.3.

$$\sigma_F = \left(\frac{2E\gamma}{\pi c}\right)^{\frac{1}{2}} \tag{3.3}$$

Using this equation, the conditions for critical stress can be determined as a function of the material and preexisting flaw size. It also shows that stresses under the critical value σ_F will not lead to unstable growth of the crack. Thus, the Griffith crack equation can be used to determine a function for the effective bonding strength of a material microstructure.

3.1.4 Current Methods of Simulating Impact Damage on TBCs

The majority of numerical methods related to damage and fracture mechanics were designed to be used with traditional engineering materials, such as metal or plastics. Therefore, making the assumption that all materials can be considered homogeneous and generally isotropic was perfectly reasonable. However, these assumptions do not hold in the case of highly porous ceramics.

To overcome this challenge, most researchers have attempted to adapt the standard continuum-based methods to include thermal barrier coatings, using techniques like effective properties, modified constitutive equations and fitting models to experimental observations. However, as is made obvious by Figure 2.6, thermal barrier coatings are anything but continuous. While some of these modifications have been successful at generating material properties that match experimental testing, they all require the use of specialized heuristics which do not conform with actual damage processes for thermal barrier coatings.

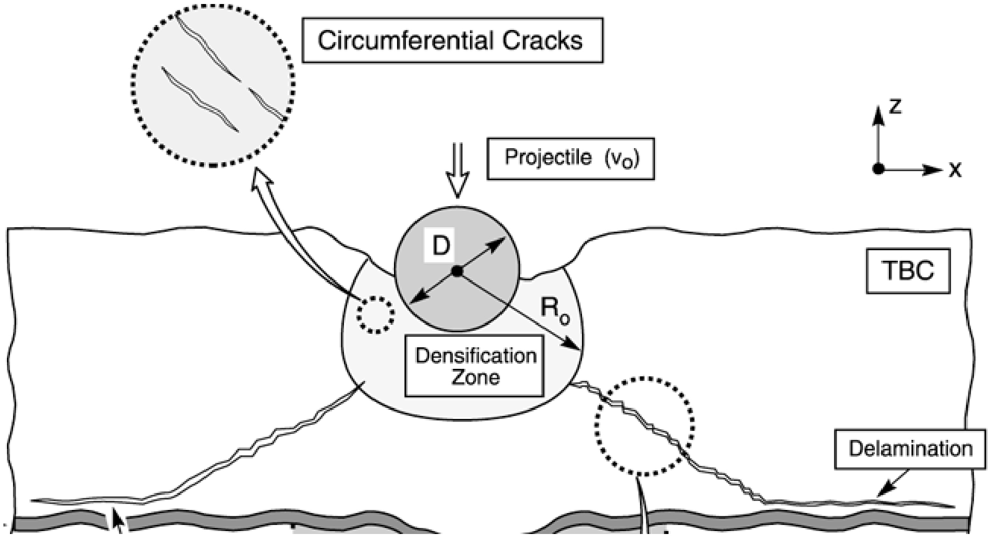

Figure 3.4: Examples of the experimental observations often included in numerical analyses of impact damage on thermal barrier coatings based on continuum approaches [7].

The first of these adaptions to classical continuum methods is the addition of effective properties. A continuous solid cannot include microstructural flaws, so porosity and cracks are resolved by proportionally reducing the effective material properties. As an example, Equation 3.4 gives the method for determining the effective elastic modulus E^* as a function of porosity θ and the Poisson's ratio μ [37]. However, this approach completely ignores any effects of the microstructure. As explained in Section 2.3.2, thermal barrier coating microstructure heavily influences the extent of fracture damage due to an impact. Given the right microstructure pathways, crack propagation from a large impact can lead to spallation, where fragments of the material are ejected from the body. The subsequent volumetric damage will not be energetically consistent with the deformation of a homogeneous material, even with reduced effective material properties.

$$E^* = \frac{E(1-\theta)^2}{(1+3\mu\theta)} \tag{3.4}$$

Since the need to account for fracture has been made clear, it is sometimes accomplished by post-processing the data from continuum models. As before, the thermal barrier coating is treated as an elastic-perfectly plastic material with effective properties, meaning that the von Mises yield criterion can be applied. However, when the stress extends beyond the critical value for the onset of fracture, a crack surface is assumed to open in that region. The critical value for fracture can be determined using the Griffith criterion in Equation 3.3. This technique can be effective for describing cases when fracture occurs in a predictable fashion, such as with kink bands created by high shear stresses (shown in Figure 3.5). However, crack propagation in thermal barrier coatings is rarely so predictable. So while this adapted model will be able to predict fracture, it will not be able to do so in a realistic manner.

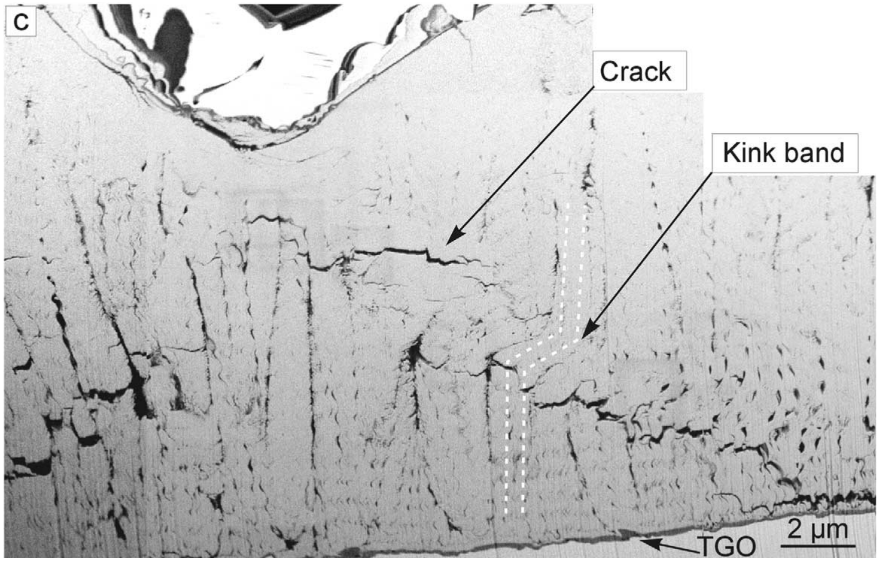

Figure 3.5: Kink bands caused by shear stress are one type of fracture damage that can be predicted using continuum methods. However, the majority of fracture damage in thermal barrier coatings is rarely as predictable. [7].

To improve the accuracy of fracture mechanics in continuum-based models, another modification is to use experimental data to tune the results. If specific types of damage processes are noted in the sample through experimental testing, the constitutive equations governing deformation in the model can be modified to match the observed damage. For example, the expression for modulus can made to degrade with accumulated damage [36]. Or to account for densification at the impact site, a constitutive model can be added to dynamically adapt the stress due to compaction in porous materials [7]. While these new models often predict damage much more accurately, they defeat the purpose of numerical analysis. Since thermal barrier coatings will vary between samples, the simulations will only be accurate when coupled with experiments for every substantially different sample. Therefore, the model cannot be used to predict the performance of new coating designs.

3.2 Introduction to the Discrete Element Method

Since continuum models are not able to adequately capture the microstructural dynamics that lead to fracture, alternative numerical methods need to be considered. One potential alternative is the discrete element method, which was first generalized by Cundall and Strack to solve problems in geomechanics [8]. The authors determined that the behavior of granular media could be modeled realistically using assemblies of spherical particles subject to contact forces. It has since been expanded to a variety of additional fields, including astrophysics, computer graphics, materials processing and damage mechanics.

The discrete element method is a meshless numerical method where dynamic particles serve as functional elements. The particles are purely a numerical construct, and act as Lagrangian nodes rather than something physical like a section of material. Nonetheless, each can be assigned any number of different physical parameters, such as radius or elastic modulus. Particles are the smallest functional unit of a discrete element model, and are used as building blocks to create more detailed geometry. Using Figure 3.6 as an example, an accurate representation of a chess piece can be recreated using simply ordered particles. Additionally, Figure 3.6 also shows that the accuracy and detail of the chess piece scales with the inverse of particle size.

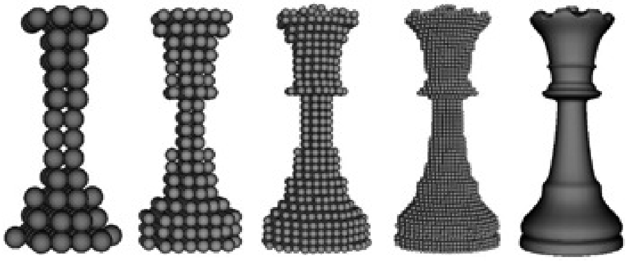

Figure 3.6: Chess pieces constructed entirely using particles as the basic building block, depicting how accuracy and detail are related to particle size [17].

Once a geometry is defined, dynamic interaction can be achieved by applying the proper constitutive equations and binding laws between the particles. One common interaction is collision, since the large number of particles makes contact situations an almost certainty. Other potential constitutive relationships include bonding functions, electromagnetic coupling and gravity. Once the forces acting on each particle have been determined, new positions and velocities are obtained by numerical integration of Newton's Second Law of Motion. As shown in Figure 3.7, this process is repeated to step the simulation forward in time.

Specifically for the case of impact damage, the discrete element method is able to produce more physically accurate results because each simulation constitutes a virtual experiment. It explicitly describes the dynamics of particle assemblies and mechanical interactions at the grain scale, where all the action occurs during deformation. In fact, the evolution of

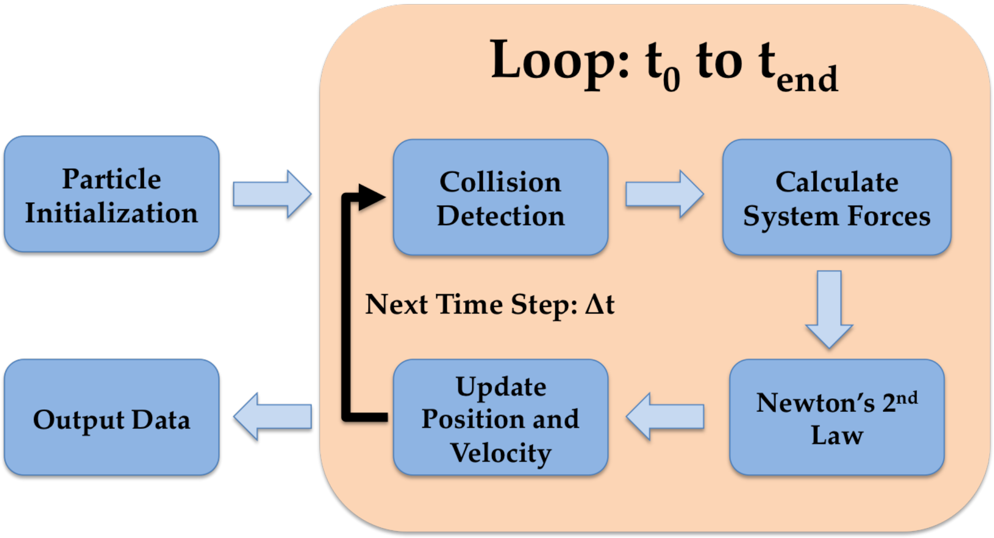

Figure 3.7: Process for setting up and solving a general discrete element model.

the material state during failure and large-scale deformation is entirely determined through simple particle-to-particle interactions. And since the microstructure is built from particles, any material heterogeneity from pores and cracks can be integrated into the solution.

As with any numerical scheme, the discrete element method has a few weaknesses. Primarily, it can be computationally expensive. A detailed simulation can have hundreds of thousands of particles, where each must be tracked for motion and contact at every time step. There are some mathematical techniques that help reduce this necessity, but stepping the simulation forward inevitably requires significant computational resources. Another challenge relates to particle assembly. The benefits of using detailed particle models of thermal barrier coatings have been made clear. However, actually constructing realistic particle assemblies can be difficult. A thorough understanding of the material microstructure and an algorithmic procedure for assembling an accurate representation using particle building blocks are both required.

Chapter 4

Simulation Design

4.1 Building a Thermal Barrier Coating with Particles

Using the concepts for the discrete element method established in the last chapter, a damage model can be developed specifically suited to impacts on thermal barrier coatings. The next several sections will walk through the steps needed to set up and solve the model.

4.1.1 Particle Properties

To create a discrete element model, the first step was to define the properties of the particles. Each was programmed with several physical parameters consistent with the type of material being represented, including the elastic modulus and surface energy. A complete list of particle properties included in the model is provided in Table 4.2. The values correspond with bulk properties of the given material, since particles are treated as continuous solids. As described in Section 3.2, all characteristics that lead to diminished material properties were created through the assembly of particles. An equilibrium bond length was also defined, which varies depending on the given material. This bond length designates the amount of separation maintained between particles when initially assembled into a model microstructure. Lastly, particle size was scaled automatically based on the total number of particles and the size of the domain. So for a fixed domain volume, increasing the detail of the model was as simple as adding more particles.

As mentioned in Section 2.2, thermal barrier coatings are made up of several functional layers, each serving a separate function. However, to simplify the model, only the ceramic topcoat was considered here. Therefore, all microstructure particles in this work were given properties representative of yttria-stabilized zirconia. But it should be noted that the model is capable of handling multiple layers of different materials. It would involve programming four separate groups of particles with the material properties corresponding to that layer. Several additional features would need to be added, such as special handing of bonding at material interfaces, adding additional complexity. This is all possible, just not in the scope of this work.

4.1.2 Microstructure Assembly

The next step was forming the particles within a defined domain, the precursor to creating an assembly representative of a microstructure. The geometry of the domain was structured as a right rectangular prism for simplicity, but could have been replaced with a different geometry. For example, many samples used in experimental impact testing of thermal barrier coatings have the shape of a thin circular plate (radius $\gg$ thickness). The dimensions of the domain were adjusted based on the type of impact, with the primary motivation of reducing edge effects. The two edges of the top face (X,Y) were given the same length, typically equal to three or more times the diameter of the impacting foreign object. Ideally, the thickness would be on the order of hundreds of microns, equivalent to the thickness of actual thermal barrier coatings. However, the number of particles needed to fill a domain of this size would be computationally prohibitive. Therefore, the thickness was typically sized at two or three times the diameter of the foreign object.

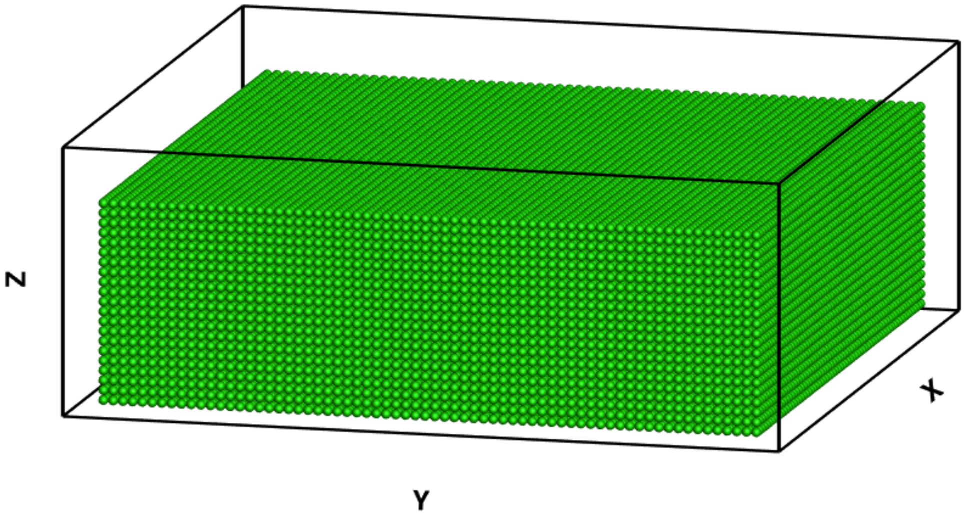

Figure 4.1: Assemblies are created by adding particles into a rectangular prism-shaped domain using the pattern shown. This initial assembly is a precursor to a microstructure, since porosity has not yet been added.

Once the domain was established, particles were added in the primitive cubic pattern shown in Figure 4.1. A densely populated domain is representative of a homogeneous material, similar to a thermal barrier coating produced without porosity. It should be noted that the particle pattern in Figure 4.1 will exhibit some anisotropy. Anisotropy was not examined in the work presented here, since all impacts with the microstructure were conducted with the same 90° orientation (perpendicular to the surface). However, this would pose a problem if the study were extended to include impacts at an angle. The topic is covered in more detail in the conclusion (Section 7.1).

Finally, the particle assembly was fixed on all sides, with the top and bottom faces kept free. A rigid boundary condition was applied to be consistent with experimental impact testing, where samples are firmly attached to the testing equipment for stability.

4.1.3 Addition of Porosity

Beginning with a fully dense set of particles, porosity and defects were added to the material through the selective deletion of particles. This was a critical step in the development of the damage model, because this was the point where all the microstructural details were added to the assembly. Selection could either be conducted randomly, or in a controlled manner to achieve a desired microstructure geometry. In the current model, selection was entirely random for the purpose of simplicity. An illustration of this process is shown in Figure 4.2. The choice of random deletion restricted the model to air plasma sprayed thermal barrier coatings, as the resulting microstructure is not an accurate representation of other manufacturing methods. Thus, if the eventual goal is to validate an entirely new process for fabricating thermal barrier coatings, a more sophisticated means of defining the microstructure geometry will be required.

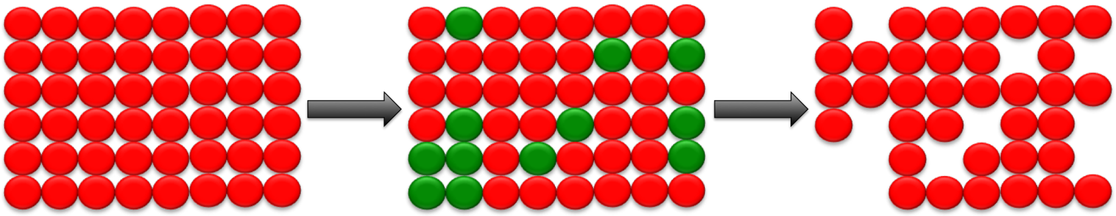

Figure 4.2: Illustration of the process employed to create a randomized thermal barrier coating microstructure. 1) Start with an ordered set of particles, representing a completely homogeneous material. 2) Particles are selected randomly, corresponding to a set volume fraction defined by the porosity. 3) Selected particles are deleted to create porosity and defects.

The amount of porosity added to the particle assembly was kept as a user-defined variable of the model. Specified as a percentage of the volume, the given porosity was used to define the number of random particles to be selected for deletion. Porosity emerged as one of the more important variables of the model, as it heavily influences the properties of the resulting microstructure. Figure 4.3 gives an example of a particle assembly that has been modified to include porosity and defects.

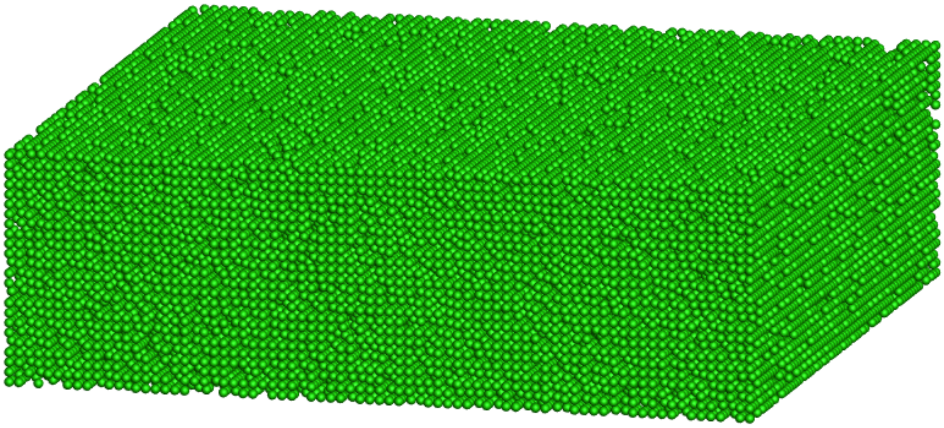

Figure 4.3: Microstructure assembly after porosity and defects have been added by the selective deletion of particles. This example includes 30% porosity, distributed randomly.

4.1.4 Particle Bonding

With particles in place, the final step to produce a functional model of thermal barrier coating material was to bond them all together. Each particle was connected to all adjacent neighbors, excluding those deleted to create porosity. A two dimensional representation of the bonding configuration is shown in Figure 4.4. Each particle could have a maximum of twenty-six bonds, each acting independently.

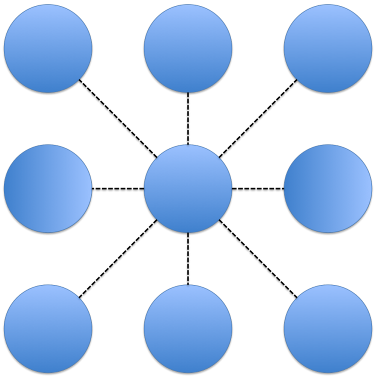

Figure 4.4: Particles are bonded with all adjacent neighbors in the configuration shown here. When expanded into all three dimensions, it equates to 26 potential bonding locations.

During the assembly process described in Section 4.1.2, particles were separated from adjacent neighbors by a length corresponding to the equilibrium distance of the bond (more detail on this in Section 4.2.2). This ensured that each bond started in a relaxed state. However, as shown in Figure 4.4, the equilibrium length varied depending on particle positions.

Once completed, a fully bonded particle assembly represents the final form of the damage model. Shown in the first image in Figure 4.5, fracture can be recreated by particle motion and breaking bonds. The second image gives an example of how a group of particles can simulate spallation by separating from the rest due to selective bond rupture. Similarly, densification of the microstructure will occur as particle bonds compress, and particles are forced into pore regions.

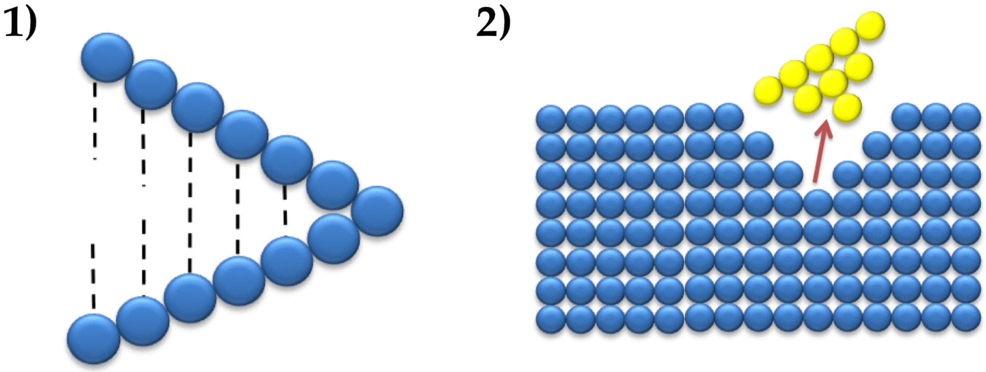

Figure 4.5: Examples of bonded particles simulating common forms of impact damage. In the first image (left), crack propagation is created by breaking bonds. In the second (right), a group of particles spalls off from the rest of the assembly.

4.1.5 Foreign Objects

With the damage model completed, foreign objects were needed to serve as impact projectiles. As with the rest of the model, the geometry of the foreign object was approximated as a spherical particle. If the cylindrical or cubic shape were preferable instead, either could have been assembled using particles as building blocks. Much like the particles themselves, the properties of the foreign object were parameters that could be altered to produce a different simulation outcomes. Radius, density, impact angle and initial velocity were all user-defined variables. A list of the most common parameter values is shown in Table 4.1. Figure 4.6 gives an example of a foreign object before undergoing a 90 ° impact with the microstructure.

4.2 Constitutive Relations for Particle Forces

All particles in the system, including the foreign object, were subject to a variety of contact forces. These forces stemmed from the physical interactions that occurred at the

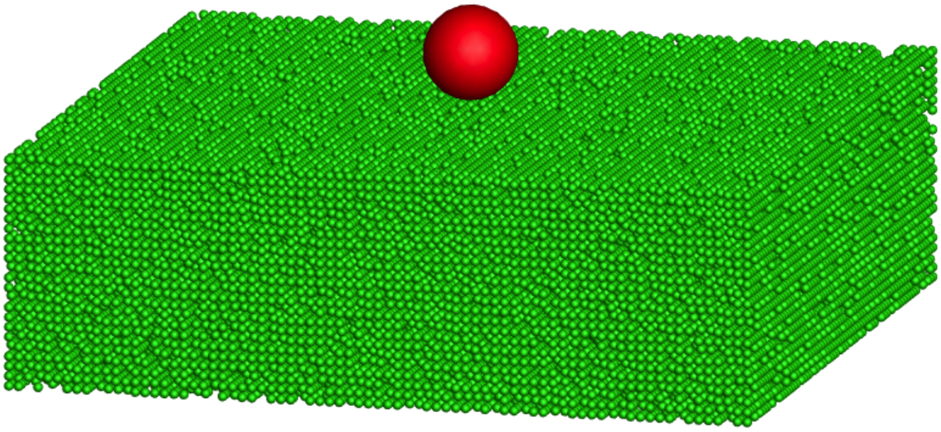

Figure 4.6: Example of a simulated foreign object set to impact the surface of a thermal barrier coating particle assembly.

Table 4.1: Commonly used parameters for defining the impacting foreign object.

Shape	**Density**	**Radius**	**Angle**	**Velocity**
Spherical	8000 kg/m^3 (steel)	$\frac{1}{4}$ inch	90°	100 m/s

particle level, and include collision, bonding, and damping forces, such as friction. The particle dynamics that emerged from the influence of these forces literally shaped the ensuing damage formation within the material.

Expressed in the form of an equation, the total force experienced by each particle was defined as the sum of the individual contact forces acting upon it. The expression for the net force acting on each particle is defined by Equation 4.1.

$$F_P = \sum F_C + \sum F_B + F_D \tag{4.1}$$

From Equation 4.1, $\sum F_C$ is the sum of contact forces caused by collisions with the foreign object or other particles, $\sum F_B$ is the net restorative force exerted by all intact bonds, and F_D is a damping force representative of non-conservative interactions such as friction. A more detailed treatment of the constitutive relations for each force will follow in subsequent subsections.

4.2.1 Contact Mechanics

As with any study of impact damage, contact mechanics were a major contributor to the forces which drove particle dynamics in this model. Collisions occurred between particles in many forms: between the impacting foreign object (which is itself modeled as a particle) and the particle microstructure, between bonded particles that were forced together by compression, and collisions between spalled particles and other segments of the microstructure. The framework used to handle collisions was Hertz contact theory, which describes the stresses induced by two elastic solids in contact. Hertz's theory was originally intended for quasi-static compression, where strains are kept small. However, since the derivation of Hertz contact theory starts with contact between two spheres, it was extended to handle particle impacts in a discrete element model with the addition of few simple assumptions.

The first assumption dealt with the discrepancy between the definitions of contact and impact. The impact of a foreign object into a thermal barrier coating is highly dynamic, and does not conform well to the concept of Hertzian contact, which should occur quasi-statically. However, for the case of impact between elastic bodies traveling at moderate velocities, elastic contact and elastic impact are similar enough to be treated as equivalent [9],[26]. Although foreign objects travel at high speeds, a sufficiently small time step was used to ensure the displacement still falls into the category of "moderate".

The next hurdle was the vibration caused by an impact, which cannot be resolved by Hertzian contact theory. Previous investigations have shown that the duration of impact between two spheres is long compared to the period of lowest mode of vibration of the spheres [48]. Therefore, vibrations effects due to impact can be neglected and Hertzian force-displacement laws for static conditions can be applied [52].

Finally, Hertz's simplification allows for the forces due to local deformations to be calculated by assuming each body can be regarded as an elastic half-space loaded over a small elliptical region of its surface [21]. This simplification is justifiable given three basic conditions:

1. Dimensions of contact are small compared to the dimensions of each body: $a \ll R$
2. Dimensions of contact are small compared to the radius of curvature of body surfaces: $a \ll R$, $a \ll l$
3. Surfaces in contact are perfectly smooth: $F_{friction} = 0$

with a representing the radius of the circle describing the contact area, R the radius of the contacting bodies, and l the significant dimension of the bodies in depth.

The purpose of the first two conditions is to minimize the edge effects seen by the stress field and enforce a sufficiently small contact region to allow the outside surface to seem relatively planar. These make the approximation of two spheres as half-spaces far more tractable. Additionally, the second condition ensures that contact strains remain sufficiently small to validate the use of linear elasticity. Both these conditions were met by enforcing a very small time step, which regulated the size of all contact dimensions. The third condition restricts the forces transmitted between bodies to the normal direction, to conform with the idealization of linear elasticity. This condition was met by treating particles as having smooth surfaces, allowing friction between particle bodies to be neglected. Friction was included in the form of a damping force instead.

With all the above conditions satisfied, the Hertz contact force between particles in a discrete element model could be derived. Starting with Equation 4.2, Hertz was able to characterize the pressure distribution across the contact surface between two general curved surfaces as a function of the maximum pressure p_0 [18]. The contact surface takes the form of a circle with maximum radius a. The pressure p reaches a maximum at the center of the contact ($r = 0$) and decreases to zero at the outer circumference of the circle ($r = a$).

$$p = p_0 \left[1 - \left(\frac{r}{a}\right)^2\right]^{1/2} \tag{4.2}$$

Taking the normal displacements resulting from the contact pressure, and applying boundary conditions for elastic displacement, the expression for the contact radius shown in Equation 4.3 can be developed into a function of the maximum pressure (see Johnson 1987 for full derivation) [21].

$$a = \frac{\pi p_0 R}{2E^*} \tag{4.3}$$

with E^* representing the relative modulus and R representing the relative radius, given by

$$\frac{1}{E^*} = \frac{1-\nu_1^2}{E_1} + \frac{1-\nu_2^2}{E_2}$$
$$\frac{1}{R} = \frac{1}{R_1} + \frac{1}{R_2}$$

where ν_1, E_1, R_1 are the Poisson ratio, modulus and radius for the first body and ν_2, E_2, R_2 are for the second body.

To calculate the total force P applied to both contacting bodies, Equation 4.4 sums the pressure acting over the contact area and relates it to the maximum pressure and contact radius.

$$P = \int_0^a p(r) 2\pi r \, dr = \frac{2}{3} p_0 \pi a^2 \tag{4.4}$$

Combining Equations 4.3 and 4.4, the contact depth δ can be found as a function of the contact radius. As shown in Figure 4.7, the contact depth δ is the amount of overlap between the contacting spheres, describing the amount of compression that has occurred on each body as a result of the impact.

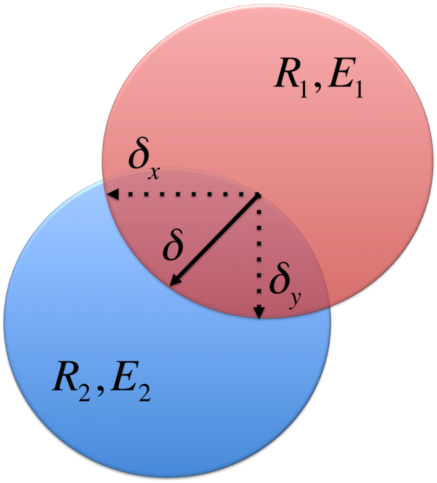

Figure 4.7: Impact of two particles, detailing the properties that are important to Hertz contact theory. δ is the contact depth related to particle overlap, R is the radius of each particle and E is the elastic modulus of each particle. The amount of overlap is exaggerated to highlight the displacement.

$$\delta = \frac{a^2}{R} = \left(\frac{9P^2}{16RE^{*2}}\right)^{1/3} \tag{4.5}$$

Finally, solving for P gives a relationship between the the amount of compression caused by the impact, and the restorative force which is generated on both bodies as a result.

$$P = \frac{4}{3}R^{1/2}E^{*}\delta^{3/2} \tag{4.6}$$

Rewriting P as F_C, Equation 4.6 gives the component of the total force due to contact, outlined in Equation 4.1.

4.2.2 Particle Bonding Force

As a first order approximation, the forces which hold a material together can be modeled as non-linear springs. Just as with a spring, these inter-atomic bonds provide a restorative force when displaced away from their equilibrium position. However, if extended beyond some critical threshold, the bond will break, leading to the creation of a new damage surface. This concept was also used to bond particles together in the discrete element model. By constructing the particle bonds using classical fracture mechanics concepts, it was shown that the resulting force functions satisfy the law of conservation of energy.

Derived from the balance between attractive and repulsive inter-atomic forces, the stress-separation plot in Figure 4.8 describes the stress σ_B required to displace bonded particles away from their equilibrium bond length, designated as b_0 on the plot. This displacement is labeled u, and defined in Equation 4.7 as the distance between the particles with the equilibrium bond length subtracted. As the bond is stretched away from the equilibrium length, the restorative stress applied by the bond increases until reaching a maximum limiting stress σ^*. Extending beyond this point leads to destruction of the bond, which occurs when the displacement passes the bond rupture separation distance δ. The total energy that is released when the bond is broken can be approximated from a material's surface energy [31]. Therefore, the area under the curve is defined as the surface energy γ_B.

$$u = x - b_0 \tag{4.7}$$

A mathematical expression for the stress-separation function was derived by approximating its shape as a half-sine curve [24] (shown in Figure 4.8), defined by the equilibrium distance b_0, the theoretical limiting stress for bond rupture σ^* and the bond rupture separation distance δ. The result is Equation 4.8, which is valid only for $0 \leq u \leq \delta$.

$$\sigma_B = \sigma^* \sin\left(\frac{\pi u}{\delta}\right) \tag{4.8}$$

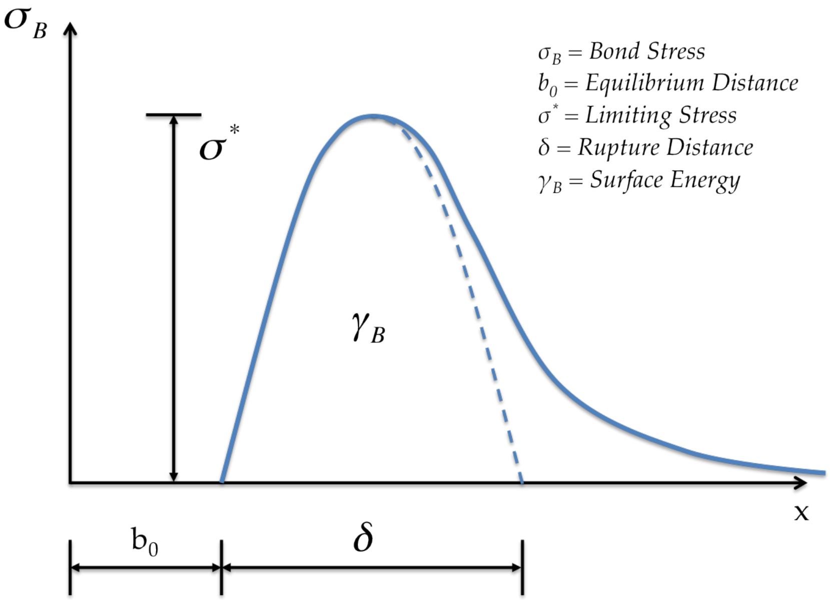

Figure 4.8: Plot of the stress-separation function derived from the balance between attractive and repulsive inter-atomic forces. It describes the stress response σ_B following any displacement of bonded particles away from their equilibrium bond length b_0, up to the maximum limiting stress σ^*. Once the displacement extends beyond the rupture distance δ, the bond is broken.

Although the limiting stress and rupture distance are properties of the material, they are not easily measured. Luckily, both quantities can be expressed in terms of known properties.

For a small displacement, the elastic modulus can be estimated from the slope of the stress-separation curve using Hooke's Law. This gave an expression relating the limiting stress σ^* to the elastic modulus E and rupture distance δ, the two unknowns.

$$E = b_0 \frac{d\sigma_B}{du} = \left(\frac{\pi b_0}{\delta} \right) \sigma^* \tag{4.9}$$

Next, the surface energy of the broken bond is equal to the area under the curve. This gave a second equation that contained the elastic modulus E and rupture distance δ.

$$\gamma_B = \int_0^\delta \sigma_B \, du = \left(\frac{2\delta}{\pi} \right) \sigma^* \tag{4.10}$$

Now with two equations for the two unknowns, Equations 4.9 and 4.10 were combined into two new expressions for the elastic modulus and intrinsic surface energy. These new expressions are given by Equations 4.11 and 4.12, and are defined entirely by known or easily measurable properties.

$$\sigma^* = \left(\frac{\gamma_B E}{2 b_0} \right)^{\frac{1}{2}} \tag{4.11}$$

$$\delta = \left(\frac{\pi^2 \gamma_B b_0}{2E} \right)^{\frac{1}{2}} \tag{4.12}$$

Plugging these two expressions back into Equation 4.8, the result was a function relating the bond stress to displacement distance.

$$\sigma_B = \left(\frac{\gamma_B E}{2 b_0} \right)^{\frac{1}{2}} \sin \left(\left(\frac{2E}{\gamma_B b_0} \right)^{\frac{1}{2}} u \right) \tag{4.13}$$

Since stress is just force per unit area, Equation 4.13 was converted to an expression for the bond force instead by multiplying both sides by the bond area A_B. The bond area is defined as the interfacial area between the two surfaces bonded together. In the case of the model, it was calculated as the square of the particle diameter, since the particle represents a general unit of material rather than a spherical volume. Thus, the bond area served as a scaling parameter, which adjusted the magnitude of the force in accordance with the size of the particle. That way, if the particles were made smaller to capture more detail in the microstructure, the material didn't become artificially stronger due to the greater number of bonds.

The final result is given by Equation 4.14, which defines the bonding component of the total force outlined in Equation 4.1. A plot of the force exerted by a single bond, as a function of displacement away from its equilibrium positions is shown in Figure 4.9.

$$F_B = A_B \left(\frac{\gamma_B E}{2b_0}\right)^{\frac{1}{2}} \sin\left(\left(\frac{2E}{\gamma_B b_0}\right)^{\frac{1}{2}} u\right) \tag{4.14}$$

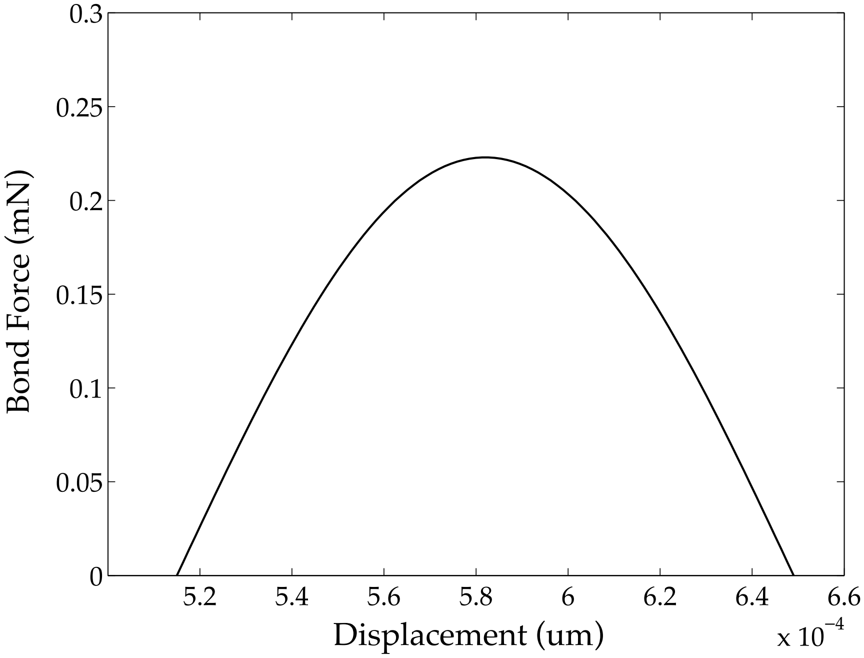

Figure 4.9: Plot of the restorative force exerted by a single bond, as a function of displacement away from its equilibrium position.

4.2.2.1 Validation of Bonding Force

The validity of the bond function derived from the stress-separation relationship was established using classical fracture mechanics. Starting with the Inglis equation for the stress at a crack tip, Equation 3.2 defines the stress concentration at a crack tip of known geometry due to an externally applied load [19].

$$\frac{\sigma_c}{\sigma_a} = 2\left(\frac{c}{\rho}\right)^{\frac{1}{2}} \tag{4.15}$$

where σ_c is the stress at the crack tip, σ_a is a uniform stress applied externally, c is the length of the preexisting crack and ρ is the radius of curvature of the crack tip. A diagram of the crack geometry for the Inglis equation is shown in Figure 3.2.

Considering the case where a sufficient external load is applied to initiate crack extension, σ_a becomes σ_F. Solving for that variable, we have the following expression.

$$\sigma_F = \frac{1}{2}\sigma_c \left(\frac{\rho}{c}\right)^{\frac{1}{2}} \tag{4.16}$$

Since crack extension severs inter-atomic bonds previously connecting the new damage surface, the stress at the crack tip σ_c during extension must be equal to the maximum limiting stress σ^* shown in Figure 4.8 [24]. Plugging in Equation 4.11 as the stress at the crack tip results in Equation 4.17.

$$\sigma_F = \frac{1}{2}\sigma^* \left(\frac{\rho}{c}\right)^{\frac{1}{2}} = \left[\left(\frac{\pi\rho}{16b_0}\right)\left(\frac{2E\gamma_B}{\pi c}\right)\right]^{\frac{1}{2}} \tag{4.17}$$

Equation 4.17 has the same form as the Griffith strength equation, which details the conditions for when material failure occurs. If $\rho = \frac{16b_0}{\pi}$, then the two match exactly. This, of course, is not a fortuitous coincidence. The concept of Griffith energy-balance at a crack-tip was "integrated" into the derivation of the force function. Conforming to the Griffith equation ensured that the bond force function satisfied thermodynamic equilibrium. Therefore, the force function in Equation 4.14 also satisfied the law of conservation of energy.

4.2.2.2 Remark on the Lennard-Jones Potential

When describing material bonds, the Lennard-Jones potential is commonly chosen as the initial starting point. As can be seen in Figure 4.10, it describes the potential energy generated by attractive and repulsive weak forces acting between molecules. In this work, the bond force function from Equation 4.17 was used instead, because it intersects with classical theory. However, comparing the derivative of the Lennard-Jones potential with Figure 4.8, it becomes obvious that the two functions actually describe identical force-separation phenomenon. The mathematical dissimilarity arises from the application of different curve fitting methods.

The Lennard-Jones potential could have been used as a replacement for the bond force derived from the force-separation approximation in Equation 4.8. However, the end result would have been quite similar and the parallels to Griffith energy balance concepts would have been lost.

4.2.3 Damping Forces

Since the damage model presented is highly dynamic, with thousands of moving particles subject to forces from all directions, the system could potentially drift into uncontrollable oscillation. This could prevent the particles from settling into a final position. While the situation is common in numerical simulations, this is problematic because it would be impossible to extract any meaningful information from a system not in equilibrium. The solution

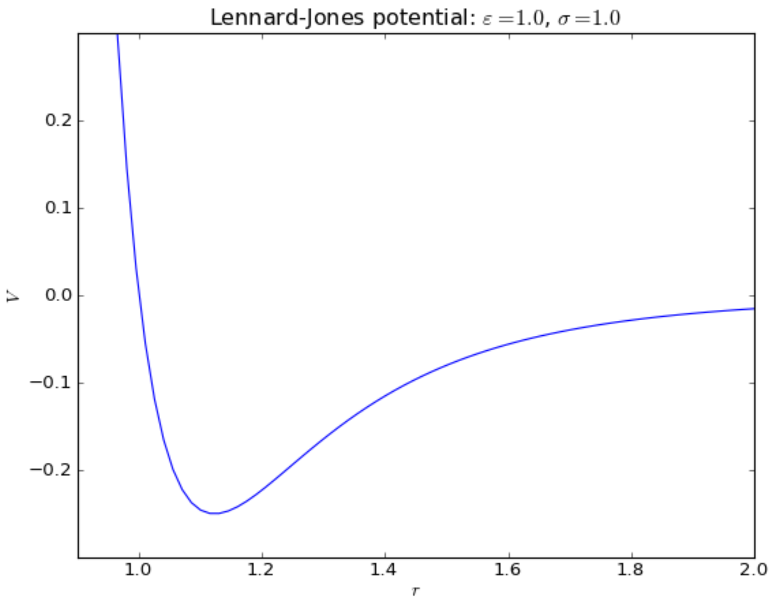

Figure 4.10: Example plot showing the Lennard-Jones potential, as a function of displacement [34].

was to introduce a damping force to dissipate kinetic energy. From a physical perspective, this type of damping is equivalent to non-conservative phenomenon such as friction and elastic wave scattering.

Since damping would occur at every time step, the damping force needed a form that was independent of the number of steps in the simulation. If defined only by static properties of the material, like in the case of friction, then the amount of damping applied in total would increase with smaller time steps. A better method was to scale the damping in proportion to the net force applied to each particle from bonding and contact. Thus, the total damping would remain constant with a diminishing time step, as the net force per time step would also be reduced. An expression for a damping force that includes this feature is shown in Equation 4.18, and was applied independently to each vector direction for every particle.

$$F_D = -\alpha sign(V)|F| \tag{4.18}$$

From the equation, $|F|$ is the magnitude of the net force, $sign(V)$ is the sign (positive or negative) of the particle velocity in that vector direction and α is the damping coefficient. Including a term for the sign of the velocity guarantees that the damping force always acted to reduce the kinetic energy of the system. The damping coefficient is used to scale the amount of damping and is typically estimated depending on the model conditions. A damping coefficient of 0.7 is common for bonded particle models of material systems, as heavy damping is necessary to approximate quasi-static conditions [35].

4.3 Numerical Formulation

With the forces acting on each particle established, the next step was to employ a time discretization scheme to translate the forces into motion. From Newton's second law, the sum of the forces on each particle $\sum F_P$ could be related to the acceleration $\ddot{x}$.

$$m\ddot{x} = F_P \tag{4.19}$$

Equation 4.1 provided an expression for the net force on a particle. Substituting that in for $\sum F_P$ resulted in a second-order ordinary differential equation.

$$m\ddot{x} = \sum F_C + \sum F_B + F_D \tag{4.20}$$

Since the goal was to solve for new particle positions, Equation 4.20 was rewritten as a coupled set of first order equations by setting $x_1 = x$ and $x_2 = \dot{x}_1$. This is shown in Equation 4.21, which gave expressions for the velocity and acceleration of a particle in a form that was ready to be numerically integrated.

$$\begin{aligned} \dot{x}_1 &= x_2 \\ \dot{x}_2 &= \frac{\sum F_C + \sum F_B + F_D}{m} \end{aligned} \tag{4.21}$$

4.3.1 Runge-Kutta Method

The Runge-Kutta method is an iterative numerical scheme for finding the approximate solution to ordinary differential equations. Runge-Kutta uses a weighted average of the function slope evaluated at multiple points. While this requires additional computation compared to simpler techniques, it returns a result with lower truncation error.

A fourth-order Runge-Kutta method evaluates the slope of the function at four separate points, as shown in the example in Figure 4.11. When defined explicitly, each slope can be found directly from Equation 4.22 using just the function $f(t_n, x_n)$, time step h and initial conditions x_n.

$$\begin{aligned} k_1 &= f(t_n, x_n) \\ k_2 &= f\left(t_n + \frac{h}{2}, x_n + \frac{h}{2}k_1\right) \\ k_3 &= f\left(t_n + \frac{h}{2}, x_n + \frac{h}{2}k_2\right) \\ k_4 &= f(t_n + h, x_n + hk_3) \end{aligned} \tag{4.22}$$

Using a weighted average of the four slopes, an updated value of x_n can be calculated with respect to the initial conditions from the current time step.

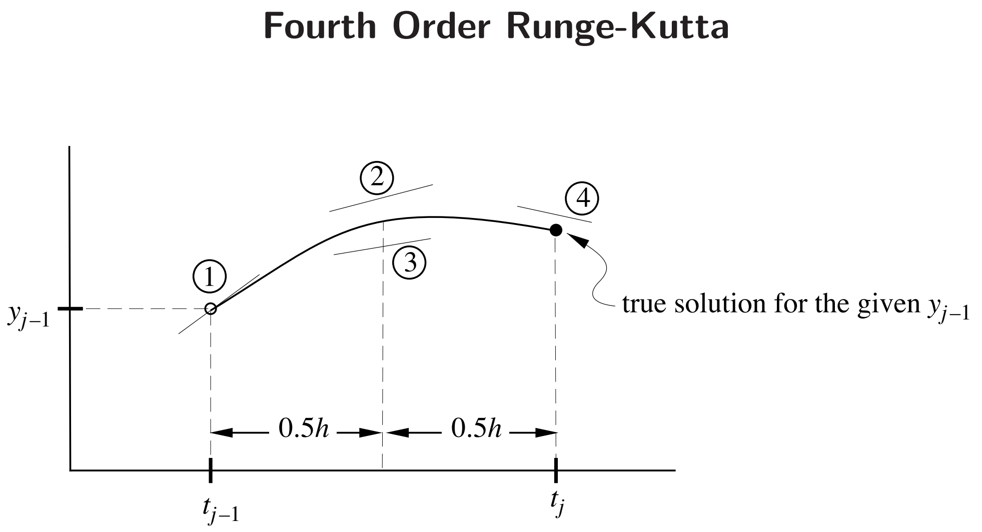

Figure 4.11: Example of how the Runge-Kutta method reduces truncation error by evaluating the slope of a function at multiple points. The slope is found four different times in this case, since the graphic is presenting the fourth-order method [38].

$$x_{n+1} = x_n + \frac{h}{6}\left(k_1 + 2k_2 + 2k_3 + k_4\right) \tag{4.23}$$

Therefore, when applied in the context of the impact simulation, Equation 4.23 was used to calculate the updated position and velocity for every particle at each time step. The slopes from Equation 4.22 were evaluated using the function defined in Equation 4.21 and the current position and velocity of each particle.

One of the benefits of the explicit Runge-Kutta method was that each stage of evaluation could be solved directly. That meant the position of a particle was updated after computing only five expressions, using known data. If an implicit method was used instead, the computation required to progress forward at each time step would have been much higher. Since the paths of all particles are coupled due to influence of collision, position updates for each time step would need to be solved for the entire particle system simultaneously.

The downside to using an explicit method was the requirement for very small time steps to guarantee numerical stability. This increased the total number of iterations required to complete the simulation, which also added to the computational cost. However, the need for a small time step was a sunk cost when dealing with impact. In order to fully capture the progression of elastic deformation during an impact, a time step must be significantly less than the time required for an elastic wave to span the smallest dimension of the domain. For a porous thermal barrier coating with a length on the order of microns, an elastic wave would cross the domain in approximately $10^{-}1$ nanoseconds. Therefore, a time step less than $10^{-}3$ nanoseconds was used for every simulation.

4.4 Results of Impact Simulation

To gain a first order assessment of the damage model described in this chapter, a basic simulation of impact damage by a foreign object was created. The parameters used in the simulation are listed in Table 4.2.

The properties in Table 4.2 were chosen to best represent the physical conditions of an actual impact scenario on a thermal barrier coating. As mentioned previously, the number of particles included was maximized to enhance microstructural detail. That maximum was often limited to 100,000 particles to ensure a reasonable computational time, which corresponded to a particle radius R of 58 nanometers for the given domain size. The elastic modulus E of the particles was set at 200 GPa, corresponding to the modulus of yttria-stabilized zirconia at high temperature. The surface energy γ was set to the value for yttria-stabilized zirconia at 1300°C [49]. The bond length δ was defined by the lattice constant of yttria-stabilized zirconia [22]. The density ρ and Poisson's ratio ν are taken from the values for bulk yttria-stabilized zirconia. These values were used for all simulations performed through the course of this work.

Table 4.2: Commonly used particle parameters for defining the microstructure in an impact simulation [49, 16, 22].

Radius R	**Elastic Modulus** E	**Surface Energy** γ	**Bond Length** δ	**Density** ρ	**Poisson Ratio** ν
58 nm	200 GPa	1.4 J/m^2	0.52 nm	6060 kg/m^3	0.25

From these figures, it was possible to observe how the damage model handles impact damage. The response of the particle microstructure matched the characteristics of an experimental impact test. When the foreign object pierces the surface in Figure 4.12, a large depression resulting from deformation is clearly visible surrounding the point of impact. Furthermore, Figure 4.13 shows clear signs of cratering, which describes the lip that forms from evacuated material around the point of impact.

While these results fit the description of a foreign object impact, observation does not constitute a sufficient form of validation. To gain a more quantitative understanding of the model performance, the next chapter covers the development of a nanoindentation simulation that uses the damage model to calculate material properties.

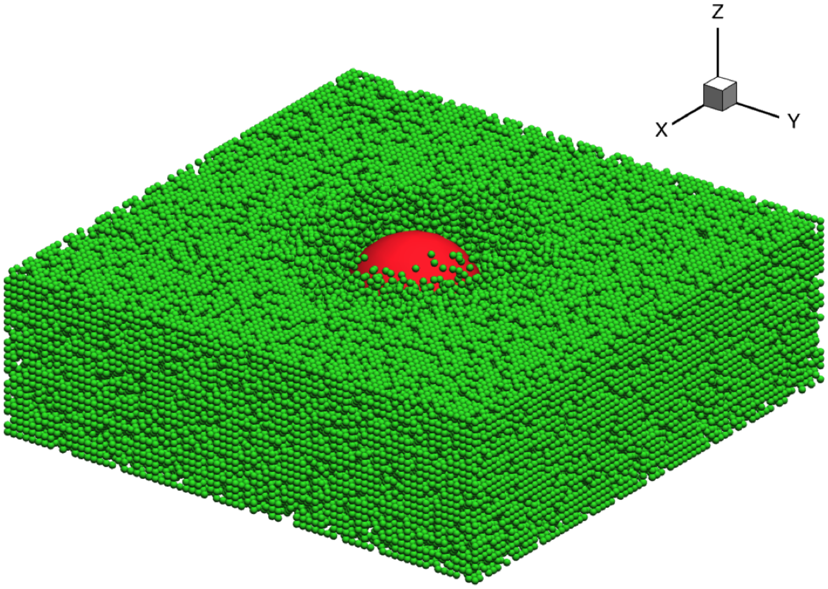

Figure 4.12: Impact of foreign object into simulated microstructure

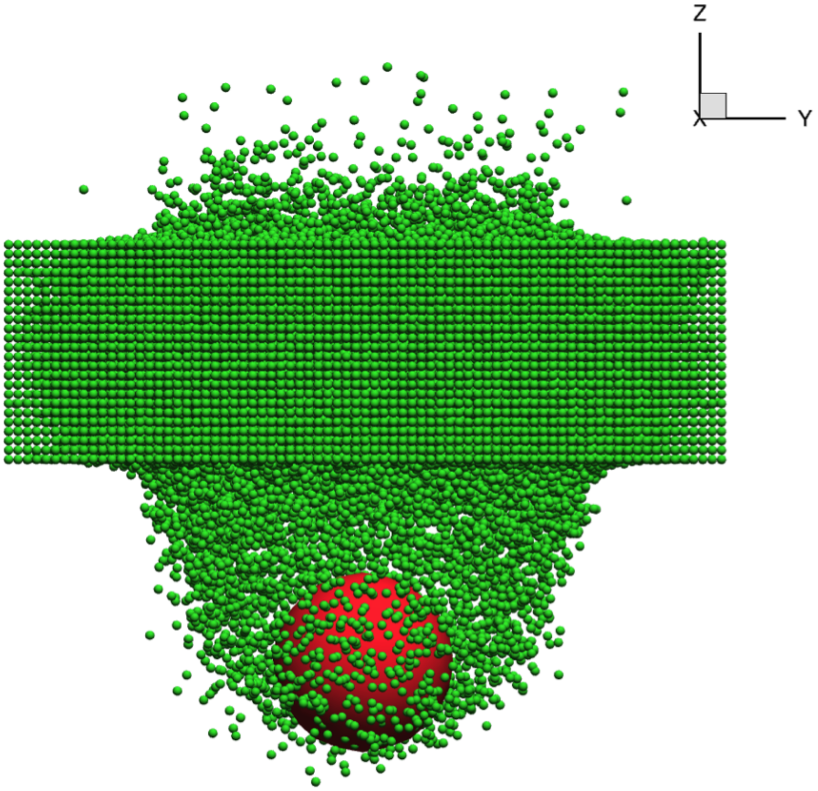

Figure 4.13: Impact of foreign object into simulated microstructure, which completely penetrates through the material

Chapter 5

Nanoindentation

One method for validating the damage model is to incorporate a standard materials test directly into the numerical model. Materials tests are an extremely common method for determining the properties and characteristics of a material. They involve the controlled deformation of an instrumented material sample, as data relating to the applied stresses and strains are recorded. The exact same methodology can be applied within a numerical simulation, where an indenter is used to deform the thermal barrier coating model, and the applied force and indenter depth are logged at every time step. That data can then be used to calculate the material properties exhibited by the thermal barrier coating model. If the material properties and characteristics generated by the nanoindentation simulation mirror those found from experimental testing in literature, it would suggest that the damage model developed for this research is indeed capable of accurately representing the damage processes inherent to thermal barrier coatings.

Although there are several materials tests that would serve the purpose of gathering comparable data, nanoindentation is uniquely suited for several reasons. For thermal barrier coatings, indentation tests are the most common method for determining the elastic modulus and hardness. Therefore, a greater volume of experimental data will be available for comparison. Beyond material property values, the indentation process produces unique damage characteristics, that vary with the material being tested. Hence, it is possible to correlate how the model results react to a changing parameter, such as an increasing applied force, compared to the known response. Nanoindentation also translates well to simulation. There are many aspects of experimental nanoindentation that require precision treatment, such as the starting position of the indenter, the closed-loop control of the applied force, and the continuous measurement of the indenter depth. However, each of these are simple to implement numerically. Finally, nanoindentation limits the required size of the computational domain, as the feature size of the experiment is very small.

5.1 Introduction to Nanoindentation

Indentation testing is a method of determining the properties and characteristics of a material sample through instrumented deformation, using an object with known properties. By measuring the protrusion of the object into the material of interest due to the application of force, accurate measurement of material properties is possible. The differentiation of nanoindentation is entirely related to scale: depths of penetration are measured in nanometers, compared to millimeters for conventional indentation tests.

The mechanics of nanoindentation testing are relatively simple. A material sample is rigidly attached to the stage of a nanoindentation testing device, which is depicted by the diagram in Figure 5.1. An indenter with known properties and geometry is placed in contact with the surface of the material, carefully avoiding any initial penetration. A more detailed discussion of indenters is given in Section 5.1.2. A steadily increasing load is then applied to the indenter, typically in set increments, until a predefined maximum force is reached. Alternatively, the indenter can be depth-controlled, where a maximum depth is specified instead. However, this method is less common and is hardware dependent. In either case, both the load and indenter depth are recorded at each increment. Before advancing to the next level of force, the indenter is held at the current state for a short period to allow the instrument to stabilize. The hold period is extended once the maximum load is reached, for the purpose of stabilizing the final depth and measuring creep within the material specimen. Finally, the indenter force is incrementally reduced back to zero, while capturing load and depth data the entire way.

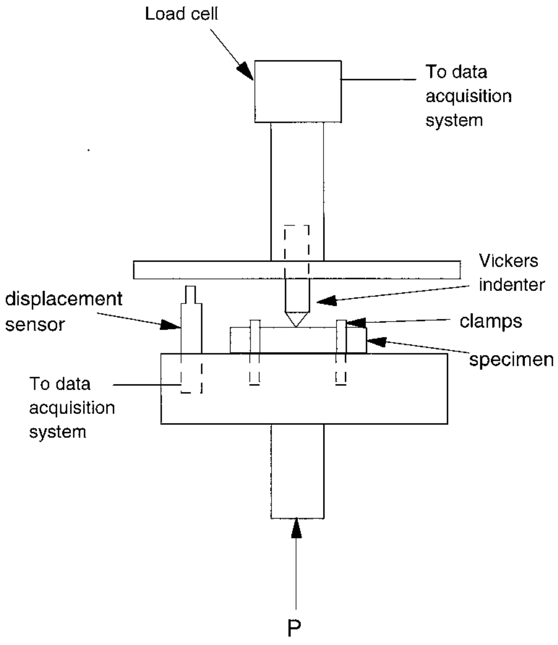

Figure 5.1: Diagram of a typical nanoindenter testing setup [3]

The size of the material specimen can vary widely, but the location of indentation must be separated from any edges or other indentations by a distance equal to at least 3-5 times the diameter of the resulting impression, in order to eliminate boundary effects [13]. Thus, the minimum size will be dictated by the size of the indenter. Similarly, the thickness should be enough to ensure that the depth of penetration does not exceed 20% of the total. Since the maximum depth generally remains on the order of hundreds of nanometers, nanoindentation can successfully accommodate thin films such as thermal barrier coatings.

The choice of the maximum applied force can be somewhat arbitrary. Applying too great a force will cause the rapid onset of fracture damage, which will effect the measured material properties. It is difficult to estimate amount of force where this transition occurs, as it depends on the material, sample thickness, indenter shape, and existence of preexisting flaws. Hence, the typical route to determining the ideal maximum force is through trial and error. The force is increased iteratively, until samples begin to fracture regularly. At that point, the threshold has been crossed, and the maximum force is set to some value below that value.

5.1.1 The P-h Curve

Nanoindentation enables the simultaneous in-situ measurement of load (P) and depth of penetration (h) by an indenter on small volumes of material. The three-dimensional stress state beneath the indenter makes the resulting P-h curves representative of the average mechanical response of that specific material in different directions. Hence, the analysis of P-h curves serve as a fundamental tool in the evaluation of the mechanical properties such as the elastic modulus and hardness.

The P-h curve is created by plotting the indenter load and depth data gathered during nanoindentation testing. An example displaying the characteristic shape and important parameters of the curve is shown in Figure 5.2.

Since loading has a non-linear effect on the indenter depth, the first important parameter is the maximum depth h_{max}, which corresponds to the maximum applied force P_{max}. The relationship between h_{max} and P_{max} will vary between materials, and is indicative of its resistance to deformation and overall plasticity. However, as the load is reversed, a certain amount of deformation will recover elastically. The final depth is labeled as h_f and represents the amount of inelastic deformation that remains.

The overall shape of the P-h curve can also be used to understand the material being tested. For example, pushing the indenter force beyond the material threshold can cause the rapid onset of inelastic deformation due to fracture. As seen in Figure 5.3, this phenomenon is visualized on the P-h curve as a sudden flattening of the curve. The value of this threshold can act as a proxy for the fracture strength, and will be higher for materials with a higher critical stress intensity factor.

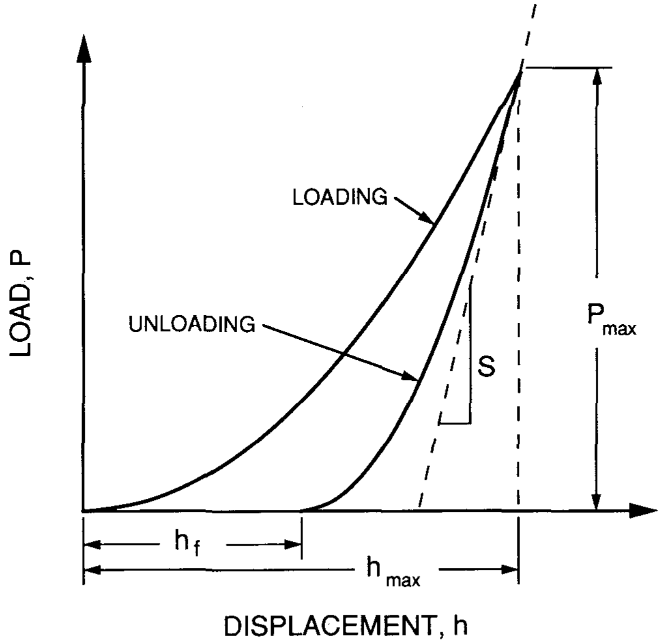

Figure 5.2: Representative plot of the load versus indenter displacement data from a nanoindentation experiment [30]. The plot is used to calculate material properties and describe material characteristics. The variables shown correspond to the following quantities - P_{max}: peak indenter force, h_{max}: the indenter depth at peak force, h_f: depth of contact impression remaining after force is removed, S: initial unloading stiffness.

5.1.2 Types of Indenters

Based on the type of material being tested and the preferred deformation response, a variety of indenter geometries are available. The most common geometries are shown in Figure 5.4, and can be separated into two categories: blunt or sharp.

From the first cases of indentation testing, spherical indenters (illustrated in Figure 5.4a) have been the de facto choice for blunt geometries [46]. Since the initial contact force is distributed over a larger area, spherical indenters provide a smooth transition from elastic to inelastic deformation. This characteristic makes them ideal for testing soft materials, or materials which are prone to fracture damage. The clearly defined elastic region of the resulting P-h curve provides a more accurate representation of material properties, such as the elastic modulus. An example of the impression left by a spherical indenter is shown in the left image of Figure 5.5.

Sharp indenters are characterized by a pyramidal geometry with a pointed tip, and are widely utilized in indentation testing. The most common are Vickers and Berkovich indenters, depicted in Figures 5.4c and 5.4d respectively. In contrast to their blunt counterparts, the pointed tips of sharp indenters induce plastic deformation soon after the commencement

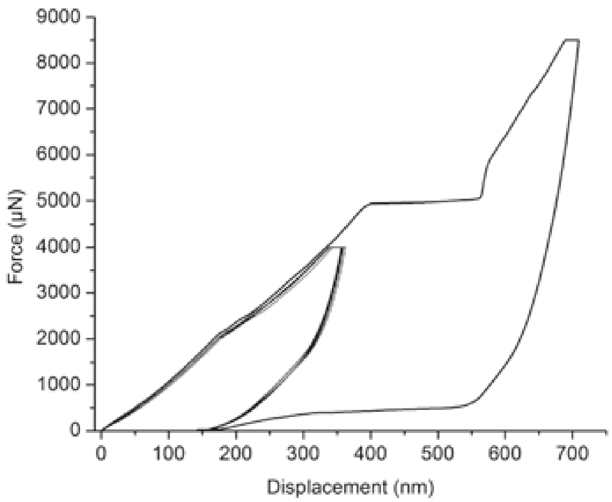

Figure 5.3: Example of a P-h curve showing the onset of rapid deformation caused by fracture, visualized by a sudden flattening of the curve [13].

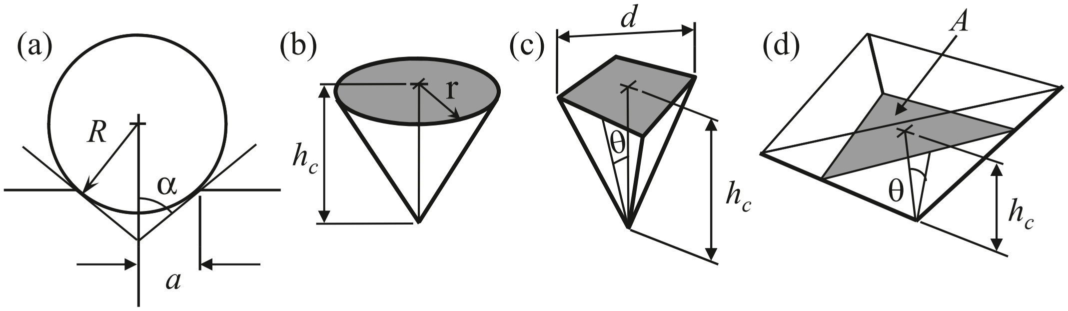

Figure 5.4: Comparison of common indenter geometries used in nanoindentation (not to scale) [13]. From left to right, the names of each are: (a) spherical, (b) conical, (c) Vickers, (d) Berkovich. The variables shown are the relevant geometric parameters of each indenter.

of contact [3]. This is useful for harder materials, or when probing for material properties related to plasticity. However, sharp indenters can be problematic in the case of nanoindentation, where the small tip size may induce inelastic deformation at extremely small loads, making it difficult to probe the elastic regime accurately [2]. An example of the impression created by a Berkovich indenter is shown in the right image of Figure 5.5.

To limit the measurement inaccuracy caused by deformation in the indenter tip, indenters are made from hard materials, typically diamond or sapphire. Indenter tip sizes range from hundreds of nanometers to a couple microns, with spherical indenters occupying the upper range.

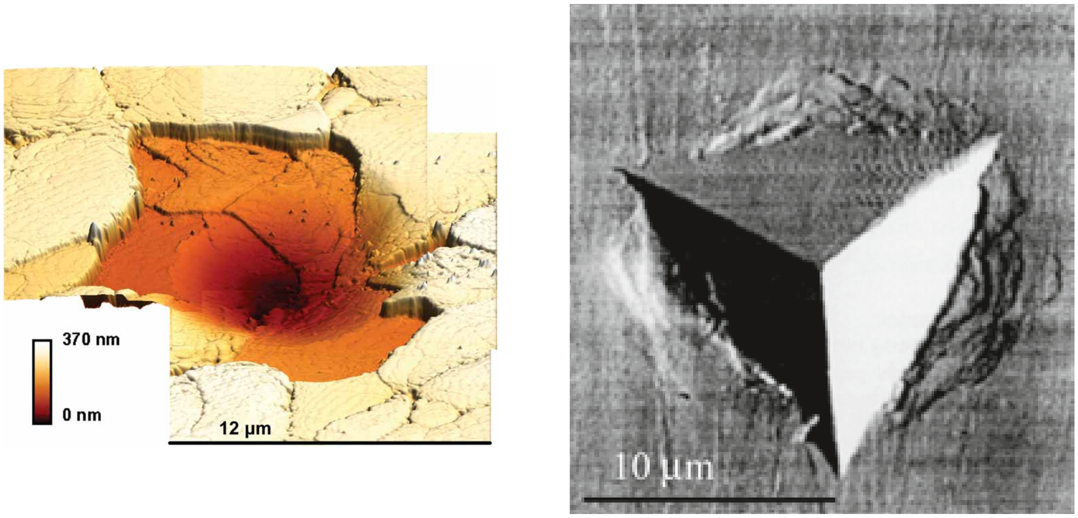

Figure 5.5: Left - AFM image of impression left by a spherical indenter on YSZ, following an indentation test [14], Right - AFM image of impression left by a Berkovich indenter, following an indentation test [13]

5.2 Determination of Material Properties

5.2.1 Calculation of Elastic Modulus

The elastic modulus is a common metric for measuring the stiffness of an engineering material, due to its universal comparability and simple testing methods. It represents a measure of a material's tendency to deform elastically when a force is applied. As such, it is relevant to the durability of thermal barrier coatings and its ability to withstand residual stresses from thermal expansion, which occur between coating layers.

Nanoindentation tests were designed for the purpose of measuring the elastic modulus from thin layers of material, such as a thermal barrier coatings. Due to the small size of nanoindenters, the material domain is significantly larger than the final size of the indentation impression. Thus, the material surface can be considered an elastic half-space. Furthermore, once the load is relieved following the application of maximum force, the initial stage of unloading is a completely elastic process. This is an important component of nanoindentation, as purely elastic deformation data is needed to calculate the elastic modulus.

To derive an equation for the elastic modulus, we begin with the assumption of elastic contact. From the theory of elasticity, the load from the indenter, which is distributed over the surface of the material, can be related to the resulting vertical displacement by the relationship shown in Equation 5.1 [6].

$$P = E^* dh \tag{5.1}$$

where P is the force applied by the indenter, E^* is the relative modulus described by

Equation 4.2.1, d is the diameter of the indenter, and h is vertical displacement caused by deformation.

By taking the derivative of the load P with respect to the vertical displacement h, the result is an expression for the the stiffness S of the material. When put into the context of a P-h curve, like the one shown in Figure 5.2, the stiffness S also describes the slope of the curve $\frac{dP}{dh}$.

$$S = \frac{dP}{dh} = E^* d \tag{5.2}$$

In the case of nanoindentation, the diameter of the indenter is not a suitable metric for the contact area, since the area will become a function of the indenter displacement h once deformation begins to occur. Thus, using Equation 5.3, the diameter of the indenter d can be related to the projected contact area A.

$$A = \frac{\pi}{4} d^2 \Rightarrow d = \frac{2}{\sqrt{\pi}} \sqrt{A} \tag{5.3}$$

And substituting into Equation 5.2,

$$S = \frac{dP}{dh} = \frac{2}{\sqrt{\pi}} E^* \sqrt{A} \tag{5.4}$$

Finally, solving Equation 5.4 for the relative modulus gives an expression for the elastic modulus as a function of the slope of the P-h curve.

$$E^* = \frac{1}{2} \frac{\sqrt{\pi}}{\sqrt{A}} \frac{dP}{dh} \tag{5.5}$$

This result allows for the elastic modulus of the sample material to be calculated using the force and depth data gathered for the P-h curve. As mentioned previously, the region of the curve immediately following unloading of the indenter depicts elastic rebound of the material. Therefore, the stiffness S can be determined by fitting a line to the first few data points following unloading of the indenter and calculating the slope $\frac{dP}{dh}$. This is demonstrated in Figure 5.2, shown with the label S.

Thus, coupled with a measure of the indenter area, Equation 5.5 can be used to compute the elastic modulus from data generated by nanoindentation testing.

5.2.2 Calculation of Hardness

Hardness is another standard material property commonly applied to thermal barrier coatings. It describes a materials ability to resist deformation when subject to a compressive force. A large value of hardness is preferable for thermal barrier coatings, to provide resistance to impact damage and erosion.

The measured hardness is equivalent to the average pressure exerted by the indenter on the material, per unit of indented area created. Thus, as shown in Equation 5.6, the hardness is calculated by dividing the maximum applied force P_{max} by the projected indentation area A.

$$H = \frac{P_{max}}{A} \tag{5.6}$$

If the nanoindentation test is force controlled, P_{max} is simply the largest force applied during the experiment. If the test is depth controlled instead, P_{max} occurs at the maximum indenter depth h_{max} and must be measured. In both cases, P_{max} occurs immediately prior to the indenter unloading, as shown in Figure 5.2. Similarly, the indentation area A is calculated at the maximum indenter depth h_{max}.

5.2.3 Determination of Indenter Area

In both the derivations for elastic modulus and hardness, the contact area A was introduced into the final result to characterize the deformation caused by the indenter. While the purpose of the substitution is to create more generalized expressions, the determination of the contact area is not trivial.

Since the size of the residual impression left by nanoindentation is so small, it cannot be easily determined using traditional techniques. Instead, the contact area is traditionally estimated using the geometry of the indenter and final depth of penetration h_{max}, both known or measurable quantities. Based on the geometries specified in Figure 5.6, an expression for the contact area can be formed [13].

$$A = \pi \left(2R_i h_c - h_c^2\right) \approx 2\pi R_i h_c \tag{5.7}$$

From Equation 5.7, R_i is the radius of the indenter and h_c is the contact depth, defined as the distance from the point where the indenter just contacts the material to the maximum depth. Again, the contact depth h_c is not known a priori and is difficult to measure. However, it can be determined using distances which are already known or can be approximated.

Returning again to Figure 5.6, the indenter depth (h_{max} at full displacement) can be split into two separate terms: the contact depth h_c and h_a, the distance from the contact point to the original material surface.

$$h_{max} = h_c + h_a \tag{5.8}$$

The maximum depth h_{max} is a known quantity, measured during the nanoindentation process. Similarly, h_a can be ascertained from the load displacement data, using the relationship shown in Equation 5.9.

$$h_a = \theta \frac{P}{S} \tag{5.9}$$

Derived from the geometry of surface deflection caused by an elastic displacement [30], P is the load derived from the indenter, S is the stiffness of the purely elastic region following

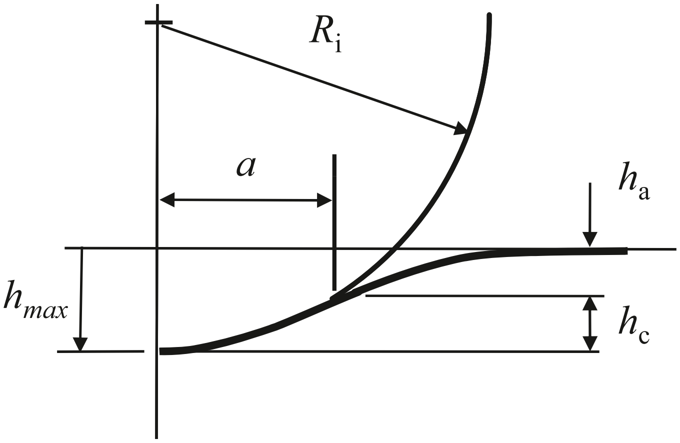

Figure 5.6: Diagram of contact between a spherical indenter and a material surface, showing relevant geometries [13]. The maximum depth of penetration is h_{max}, the contact depth h_c describes the distance from the bottom to the perimeter of contact, and h_a is the distance from the perimeter of contact to the material surface.

unloading (found for the elastic modulus above), and θ is a geometric constant for the indenter shape (equal to 0.75 for a spherical indenter).

Solving Equation 5.8 for h_c and substituting Equation 5.9 for h_a, the result is an expression for h_c in terms of all known properties. Since we're interested in the contact area at at the peak indenter force, P is set to P_{max}.

$$h_c = h_{max} - \theta \frac{P_{max}}{S} \tag{5.10}$$

Now that a fully defined expression for h_c has been found, Equation 5.10 can be substituted into Equation 5.7 to solve for the contact area A.

$$A = \pi R_i \left(h_{max} - \theta \frac{P_{max}}{S} \right) \tag{5.11}$$

By simply updating the parameters of the experiment, such as indenter geometry constant and indenter load, Equation 5.11 can be used to solve for the contact area for any type of indenter and a variety of nanoindentation testing parameters.

5.3 Integration into Simulation

The process of nanoindentation is surprisingly well suited to numerical treatment. Many of the challenges faced during experimental nanoindentation testing are related to precise control and measurement of the indenter, as it presses against the sample. The same process was comparatively simple to integrate into a simulation, because control and measurement of every component can be defined or calculated directly. To give an example, it is often impossible to initially place the indenter in contact with the material surface without causing some deformation, as required by the standard nanoindentation procedure described in Section 5.1. As a result, multiple empirical correction factors have been developed to account for this initial damage. By comparison, the initial position of the indenter was defined algorithmically in the simulation, to guarantee that contact would be made without applying any initial stress on the material.

To build the nanoindentation simulation, the procedure described in Section 5.1 was adapted almost literally into code. The indenter was force-controlled, meaning that the force applied by indenter was gradually increased up to a predefined maximum value. The indenter depth was recorded at every time step, which coupled with the known indenter force, was used to generate the P-h curves necessary to calculate material properties. Since the particle assembly in the nanoindentation simulation was still representative of a thermal barrier coating sample, the same particle parameters shown in Table 4.2 were applied.

Consistent with the rest of the model, a spherical indenter geometry was chosen for the nanoindentation simulation. However, in this case, the choice was not only motivated by simplicity. When testing materials that are particularly prone to the development of microcracks, such as plasma-sprayed ceramics, damage accumulation caused by a sharp indenter can effect the measurement of elastic modulus [3]. As explained in Section 5.1.2, sharp indenters can induce the onset of plastic deformation almost immediately on contact with brittle materials. Thus, the choice of a spherical indenter was motivated by the desire for a smooth transition from elastic to inelastic deformation, so that accurate material properties could be measured. Furthermore, data produced by spherical indenters has been shown to be in good agreement with results from the more famous Berkovich geometry [5]. The physical parameters assigned to the indenter are given in Table 5.1.

Table 5.1: Physical parameters for the indenter used for nanoindentation simulations.

Shape	**Density**	**Radius**	**Angle**
Spherical	3980 kg/m^3 (sapphire)	500 nm	90°

Since the thermal barrier coating samples used for nanoindentation testing are similar to those used in impact testing, the same particle damage model described in Sections 4.1 and 4.2 was carried over for the nanoindentation simulation. Although the size of the domain remained unchanged, a rigid boundary condition was added to the bottom of the particle assembly, in addition to the existing boundaries on the sides. Compared to impact tests, where the projectile can sometimes penetrate through the entire thickness of the material sample, nanoindentation tests are designed to only leave a small impression. Thus, samples are mounted onto a horizontal plate, and effectively confined on five sides. The additional boundary condition was added to mirror this difference.

Chapter 6

Results and Discussion

Numerical models provide the best results when utilized to inform the direction of design decisions, rather than to generate actionable data. This is especially true in the case of thermal barrier coatings, where variability in the microstructure makes the determination of an exact solution nearly impossible. Therefore, the performance of the damage model presented in this work will be measured both qualitatively and quantitatively, since matching specific material property values is not a realistic expectation.

The motivation for building a damage model using the discrete element method was the potential to capture realistic representations of physical damage processes on thermal barrier coatings. Thus, the best way to qualitatively assess the functionality of the model is by inspecting whether the damage characteristics of experimental nanoindentation tests are also present in simulation results. If the same trends are identified during the nanoindentation process, especially when varying parameters such as the porosity or indenter force, it would serve as a strong qualitative argument that the damage model is indeed depicting physically accurate results.

Of course, a quantitative performance characterization is still an important component of validating any model. Its not enough to look the part, if the numerical result do not conform to expected values. Therefore, material properties generated from the nanoindentation simulation were compared to experimental results found in literature. However, due to the inevitable variability of thermal barrier coating samples, experimental material property values were collected from multiple authors, in order to create meaningful range for comparison.

To gather the numerical data required for the analysis described above, a large number of nanoindentation simulations were computed, like the one shown in Figure 6.1. Output data were recorded in the form of P-h curves, and post-processed to determine the material properties from each of the modeled thermal barrier coating samples.

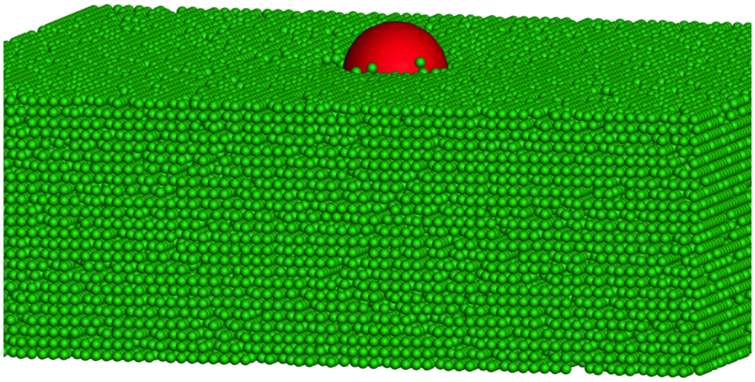

Figure 6.1: Example image of nanoindentation simulation

6.1 Nanoindentation Results

The results of each nanoindentation simulation were visualized by animating the changing positions of all particles in the system as time was stepped forward. To give an example of how the particle assembly reacted when subject to the applied indenter force, Figure 6.2 shows a storyboard of the entire nanoindentation process. Starting on the first frame, the indenter is placed just above the material and subject to a steadily increasing force. Upon contact, the force applied by the indenter causes the material surface to buckle, but stay coherent. Even as the load is increased up to the maximum force, the particle bonds are able to remain intact and apply a stabilizing counter-force, bringing the indenter to equilibrium. This outcome is consistent with an elastic response to deformation. This conclusion is further reinforced when the applied force is removed. The indenter returns to almost its initial position, signifying that little to no permanent damage remains.

Typically, thermal barrier coatings don't undergo plastic deformation. Ceramics transition from elasticity directly into brittle failure. To expose the evolution of this type of damage formed by the model, Figure 6.3 shows another nanoindentation simulation depicting a very different response. As before, the material initially responds elastically, shown by the coherent buckling of the surface in the second frame. However, once the elastic threshold is crossed, the material experiences rapid deformation leading to the indenter penetrating more deeply than in the elastic case. The cause of this shift is the onset of fracture, as particle bonds begin to break. A cascading rupture of bonds opens new damage surfaces, which can't be closed again. Even when the indenter force is removed, a depression persists, showing permanent damage to the material structure.

From the two storyboards, the damage model appears to exhibit the proper transition from elastic to inelastic damage distinctive to brittle ceramics. To dive deeper into the

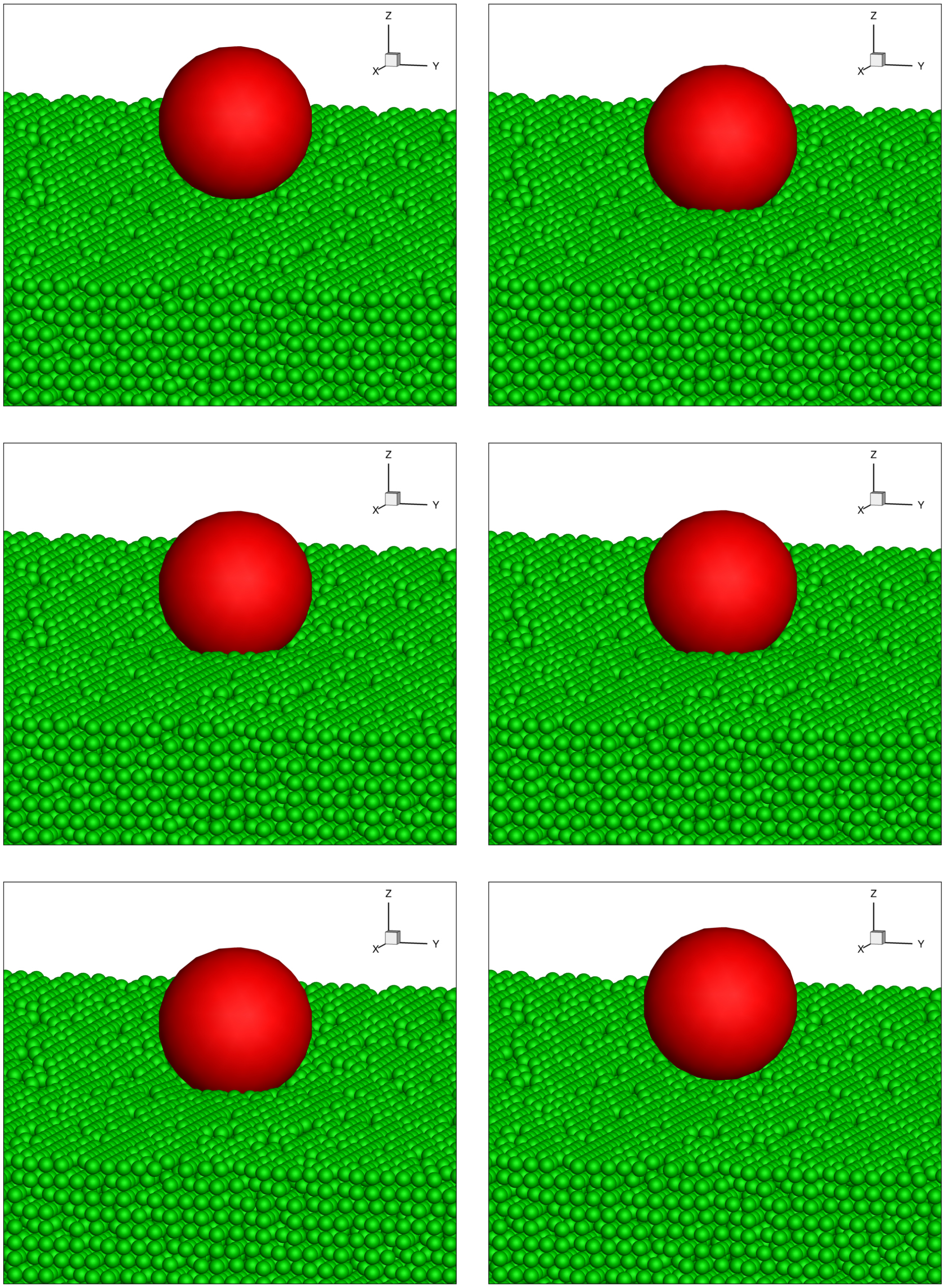

Figure 6.2: Storyboard showing model of indentation on a thermal barrier coating, in the case of a mostly elastic response

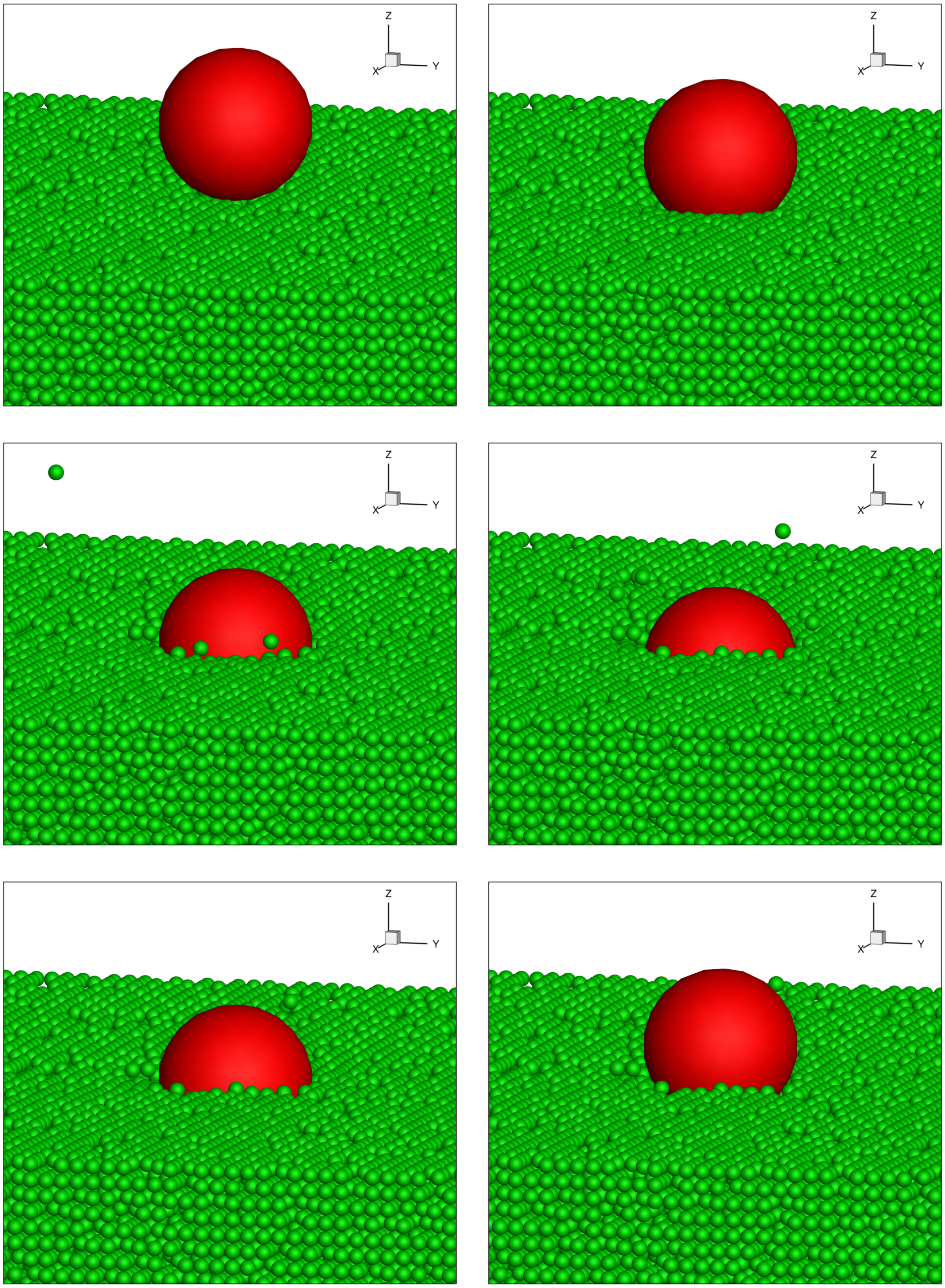

Figure 6.3: Storyboard showing model of indentation on a thermal barrier coating, in the case where the material begins to fracture, leading to visible inelastic deformation.

analysis of whether the model is accurately reproducing the damage characteristics found in thermal barrier coatings, the next step is to consider the P-h curves generated by the nanoindentation simulations. Figure 6.4 plots the force-displacement data from the mostly elastic case, shown in Figure 6.2.

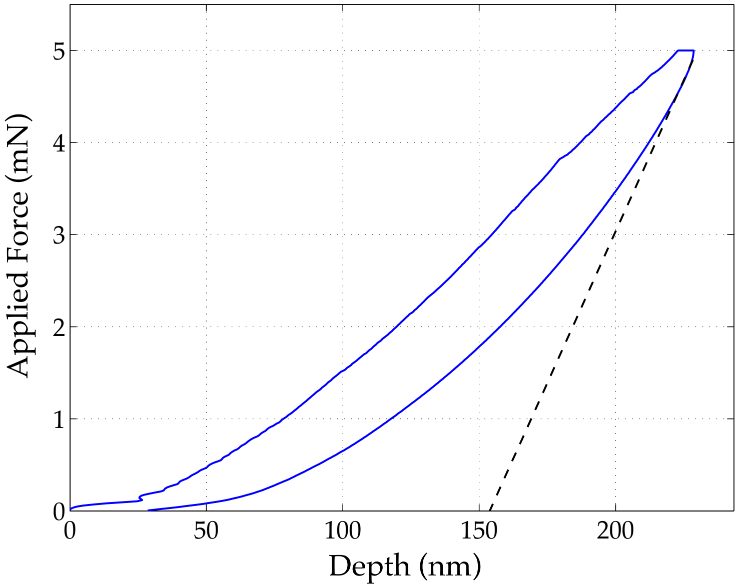

Figure 6.4: P-h curve for 100k particles, indenter force of 5mN and a porosity of 15%

The shape of the P-h curve from the elastic nanoindentation simulation fits the description given in Section 5.1.1 and is a good match to the example shown in Figure 5.2. The loading path is non-linear, requiring an increasing amount of force to push the indenter deeper. Once the maximum force is reached, the depth of the indenter recovers elastically as the indenter is unloaded. Since a small amount of inelastic deformation occurred, the unloading curve does not follow an identical path to the loading curve.

Moving on to the inelastic case, Figure 6.5 plots the P-h curve created from the nanoindentation simulation illustrated in Figure 6.3.

Comparing this result to the example shown in Figure 5.3, which depicts inelastic deformation in an experimental nanoindentation test, the similarities are immediately obvious. In both plots, the onset of inelastic deformation is marked by a horizontal detour from the expected path. This deformation remains permanently, illustrated in both examples by the incomplete recovery of the microstructure once the load is finally removed. Perhaps the most interesting observation, however, is the horizontal line itself. As detailed in Section 5.1.1, this rapid onset of inelastic deformation is characteristic of fracture damage. In the simulation result, this same effect occurs automatically, without the requirement for a subroutine

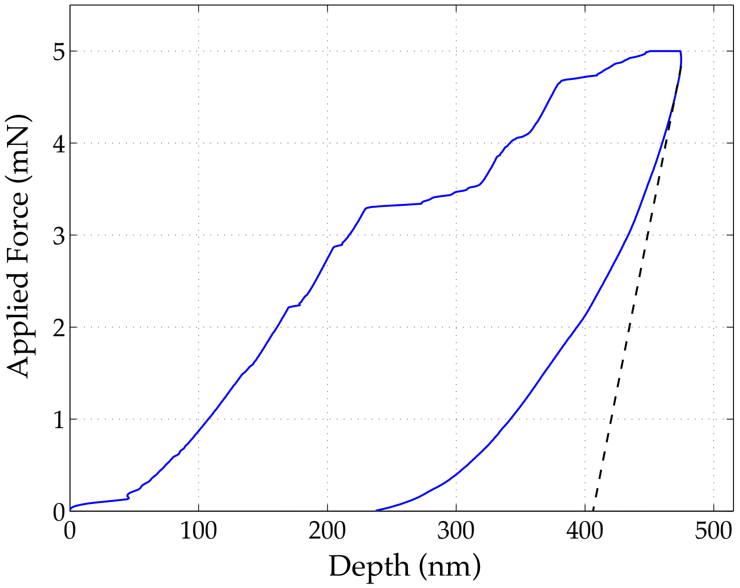

Figure 6.5: P-h curve showing an example of the rapid onset of inelastic deformation, illustrated by the horizontal divergence from the expected path. The horizontal part of the curve is indicative of fracture damage, and is commonly documented in experimental nanoindentation tests.

to initiate the process artificially. It simply corresponds to the point where sufficient stress is applied to cause particle bonds to break, just like in the real material.

6.1.1 Effects of Microstructure on Nanoindentation

Despite the two very different damage responses shown in Figures 6.4 and 6.5, both examples were produced using the same nanoindentation simulation parameters. The only difference was the selection of which particles to delete in order to create the microstructure. As will be shown subsequently, the material microstructure was one of the main factors that contributed to the material property response. This fact is illustrated in Figure 6.6.

Even though all six graphs in Figure 6.6 were created using the same model conditions and properties, the resulting indentation characteristics are quite different due to variations in the distribution of porosity. As explained in Section 4.1.3, porosity in the thermal barrier coating was created through the random deletion of particles. Thus, the propagation of deformation and broken bonds was different for each permutation of the simulation.

Since the microstructure had such a strong influence on material response to nanoindentation, it was logical to assume that the material properties would be equally affected. This was indeed the case, confirmed by Figure 6.7 for the elastic modulus and Figure 6.8 for

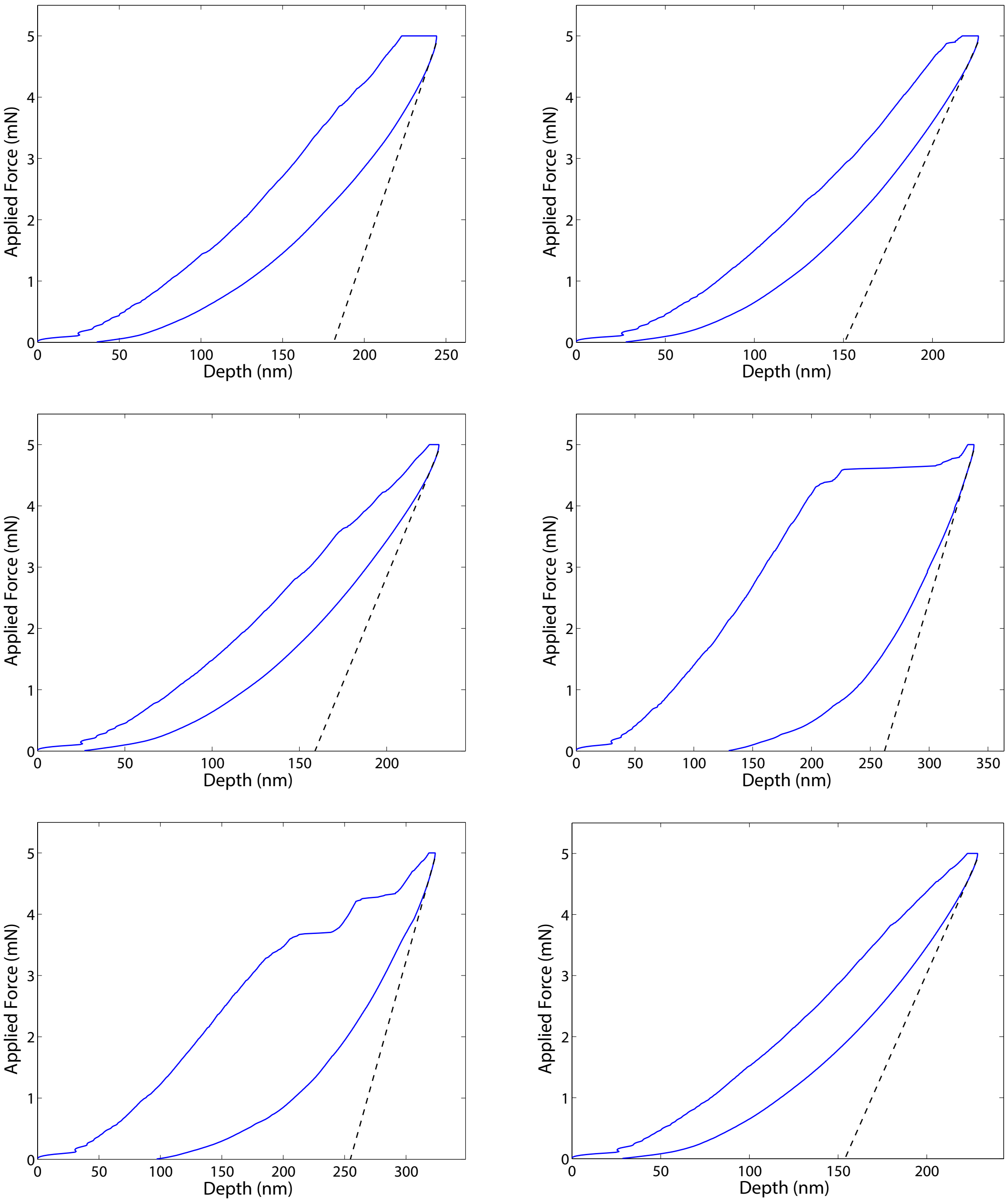

Figure 6.6: Showing different P-h curve variations and results, even for the same model conditions, due to differences in the microstructure arrangement.

the hardness. Both properties fluctuate significantly despite being generated using the same simulation parameters, save for the microstructural distribution.

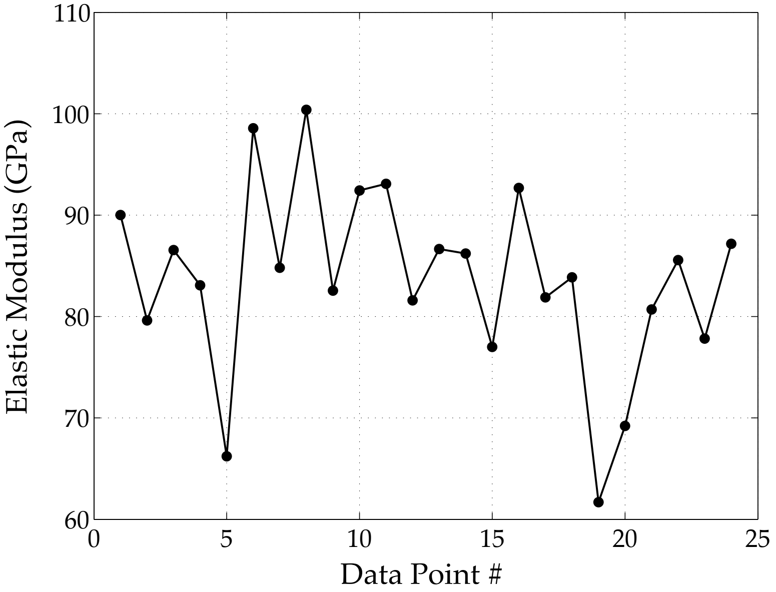

Figure 6.7: The elastic modulus data points which make up the average value for an applied force of 5mN and a porosity of 15%

To compensate for the material property uncertainty introduced by the microstructure, all values provided for the elastic modulus and hardness were averaged over a large number of simulation results. This provided values that accounted for a larger range of potential microstructure permutations, and could therefore be compared.

6.2 Analysis of Free Parameter Trends

Beyond the random placement of pores in the microstructure, the two other variables incorporated into the model were the maximum indenter force and the amount of the porosity, by volume percent. These two quantities were treated as free parameters, which could be adjusted to vary the outcome of the nanoindentation simulation. With the exception of microstructure distribution, which can't be modified when the coating is constructed using air plasma spraying, the volume percent of porosity is the single greatest influence on thermal barrier coating performance. Both in terms of thermal insulation and durability. By varying the maximum force applied by the indenter, it is possible to probe the transition between elastic and inelastic deformation. This transition has a characteristic shape, which depends on the indenter geometry, making it a good metric for comparison.

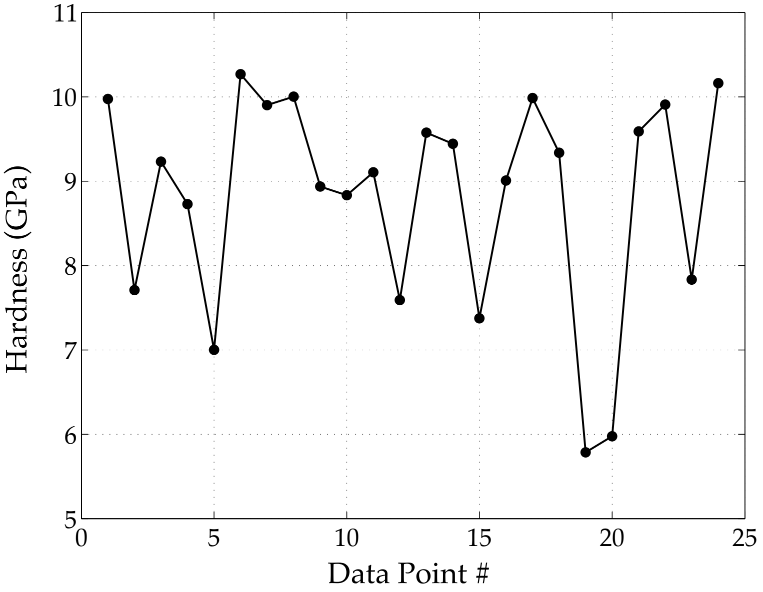

Figure 6.8: The hardness data points which make up the average value for an applied force of 5mN and a porosity of 15%

To determine whether the model could match the trends identified from experimental nanoindentation testing, both the indenter force and porosity were each independently varied while the other was held constant.

6.2.1 Varying Indenter Force

To explore the effects of increasing the applied force, simulations with the same variables and microstructure pore placement were run with increasing indenter forces. An example is shown in Figure 6.9, which depicts P-h curves for an indenter force of 1mN, 3mN and 5mN, applied to an identical microstructure with 10% porosity. The deformation depicted by all three curves remains primarily in the elastic regime, leading to maximum depths and curve "sizes" corresponding roughly proportional to the applied force. For the loading component of the curves, the paths line up very closely, even though the max applied force is different. In fact, the visible deviation may be an artifact of the simulation method, since a set number of time steps were used irrespective of the load. Thus, the amount of increase in the indenter force per step will be much smaller for the 1mN example compared to 5mN. This congruency demonstrates the reversibility of elastic deformation in the microstructure model, shown specifically in the case of indentation, and is consistent with findings in experimental nanoindentation tests [2], [39]. As expected, the unloading portions follows a different path in accordance with the amount of inelastic deformation induced at maximum load.

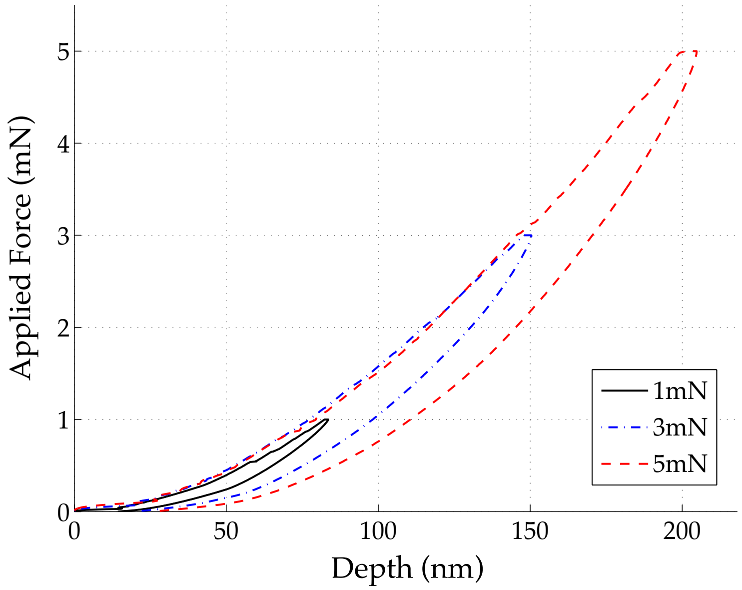

Figure 6.9: P-h curve for increasing indenter force, showing the fully elastic case. As they should, curves closely line up during loading.

Whereas the curves in Figure 6.9 remained primarily in the elastic regime, over the entire range of applied force, Figure 6.10 shows a simulation where the thermal barrier coating begins to fracture once an indenter force of 5mN is applied. As in the elastic case, the curves line up during the initial phase of loading. However, starting at just over 2mN, several examples of indenter "pop-in" begin to occur, indicative of permanent deformation. These events continue to increase in frequency and duration as the indenter force ramps up, until sustained fracture is reached. Sustained fracture is identified by the flattened section of the P-h curve, which means an increasing amount of deformation is caused by the same applied force. The outcome, compared to the 5mN curve shown in Figure 6.9, is a notably greater maximum depth and significantly more permanent deformation.

This difference was instructive for several reasons. First, it showed that the onset of fracture happens at a critical point, after a build-up of elastic deformation. This is consistent with the concept of a critical point for the onset of fracture described by the Griffith crack criteria in Section 3.1.3, suggesting that the model was properly exhibiting the failure modes described by fracture mechanics. Secondly, the differences between the plots, despite being generated using the same applied force and amount of porosity, highlights the factors which lead to the onset of fracture. Microstructure and the placement of the bonded particles clearly had a significant role, confirming the supposition that a bonded particle model allows for damage to propagate in the direction of areas of weakness. Finally, it was observed that the transition from elastic deformation to fracture damage occurs near the 5mN threshold.

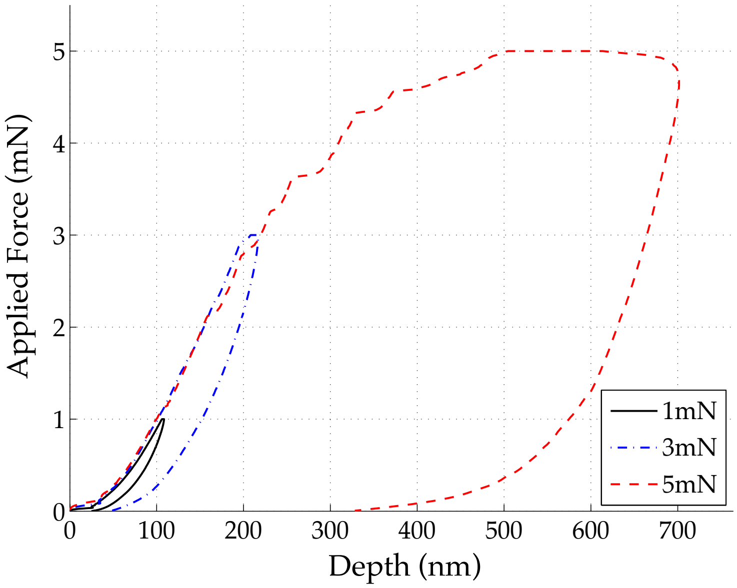

Figure 6.10: P-h curve for increasing indenter force, showing onset of fracture damage. As they should, curves closely line up during loading.

A deeper look into the data from additional permutations of the same simulation confirmed this. Knowledge of this threshold was useful when calculating material properties, such as the elastic modulus.

Next, to determine how the material properties of a thermal barrier coating were influenced by the indenter force, the elastic modulus (E) and the hardness (H) were computed with an increasing applied force. The resulting values are plotted against the indenter force in Figures 6.11 and 6.12.

Perhaps the most important observation regarding Figures 6.11 and 6.12 was that both E an H increase with indenter force, up to 5mN. This result was in conflict with the trends found from most experimental nanoindentation tests [51],[14],[42], which overwhelmingly used sharp indenters. These tests described the material properties dropping initially and leveling off at a steady value. However, the plots perfectly matched the results found from experiments conducted with a spherical indenter instead [53],[27]. The difference lies in how the indenter interacts with the material surface. As explained in Section 5.1.2, a sharp indenter will induce inelastic deformation in a brittle ceramic material at a very small applied force, breaking the bonds holding the material together and eroding its ability to resist the penetration of the indenter. Hence, the observed material properties will decrease. A spherical indenter, which was used in these simulations, elastically deforms the surface on initial contact. Elastic compression causes densification of the material, boosting its ability to resist the indenter, and as a consequence, its measured strength too. Thus, the results

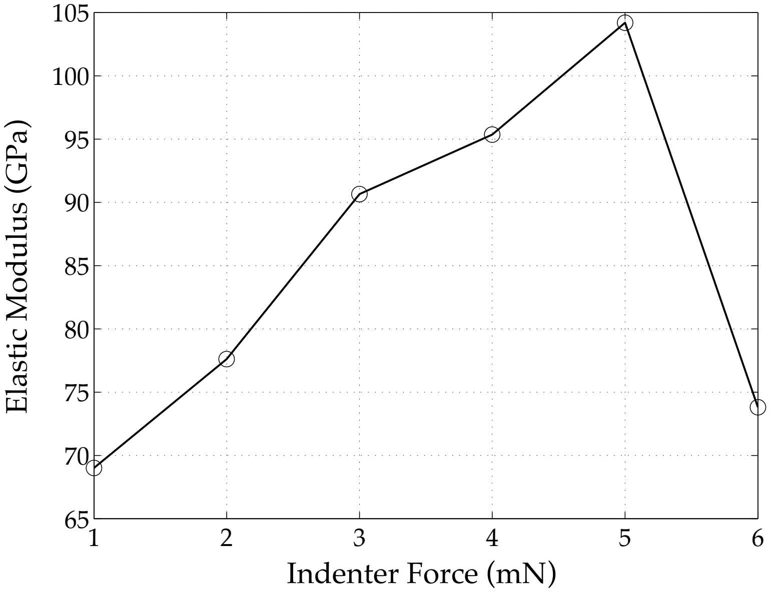

Figure 6.11: Plot of Elastic modulus as indenter force is increased

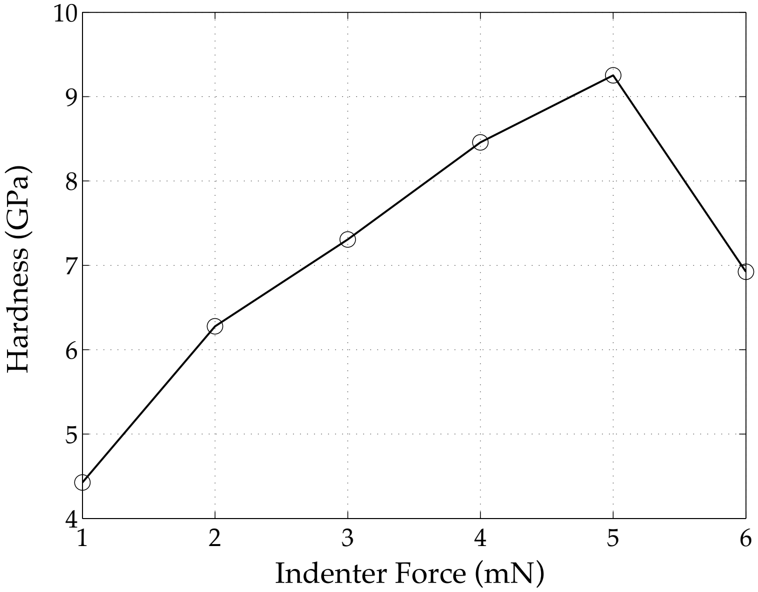

Figure 6.12: Plot of hardness as indenter force is increased

found in Figures 6.11 and 6.12 were in agreement with the expected result.

6.2.2 Varying Amount of Porosity

Similarly, increasing the porosity while keeping the indenter force constant had a recognizable effect on the resulting P-h curve. Since a reduced amount of material and bonding structure is present to withstand the force of the indenter, the indenter is able to penetrate more deeply at higher amounts of porosity. Effectively, increasing the porosity causes the P-h curve to extend to the right.

To visualize this shift, and determine whether the same phenomenon could be recreated by the damage model, the nanoindentation simulation was run with an increasing level of porosity. A constant indenter force of 3mN was applied, in order to prevent the onset of inelastic deformation, which would skew the resulting plots. A set particle arrangement (non-random particle deletion) was also maintained for all model runs, to ensure microstructural variations did not influence the outcome. The result can be seen in Figure 6.13, which closely follows the results found in experimental literature [20].

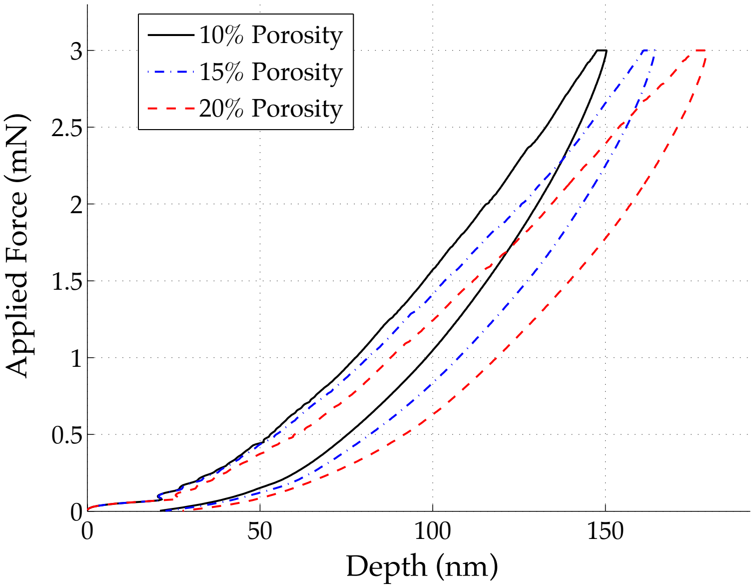

Figure 6.13: P-h curves for indenter tests with increasing porosity

From a physical materials perspective, increasing the porosity should undoubtedly lead to reduced material properties. A larger number of gaps and and cracks between splats in the microstructure will compromise interface adhesion and reduce available bonding sites. This same scenario was mirrored by the damage model. As more particles were deleted with a higher volume of porosity, the number of bonds was also reduced. Thus, less capacity was available in the system to store potential energy from bond compression and resist deformation. The expected outcome was material properties that decrease linearly with porosity, which is consistent with findings from experimental testing in literature [23, 29].

Based on the observations made regarding Figure 6.13, a reduction in material properties was a given. If an indenter is able to penetrate more deeply at the same applied force, leading to a greater indenter area, Equations 5.5 and 5.6 dictate that both the elastic modulus and the hardness will be diminished. To confirm this hypothesis, the modulus and hardness were plotted in Figures 6.14 and 6.15, while increasing the amount of porosity in the microstructure. As expected, a near linear decrease was observed for both properties, conforming with experimental results.

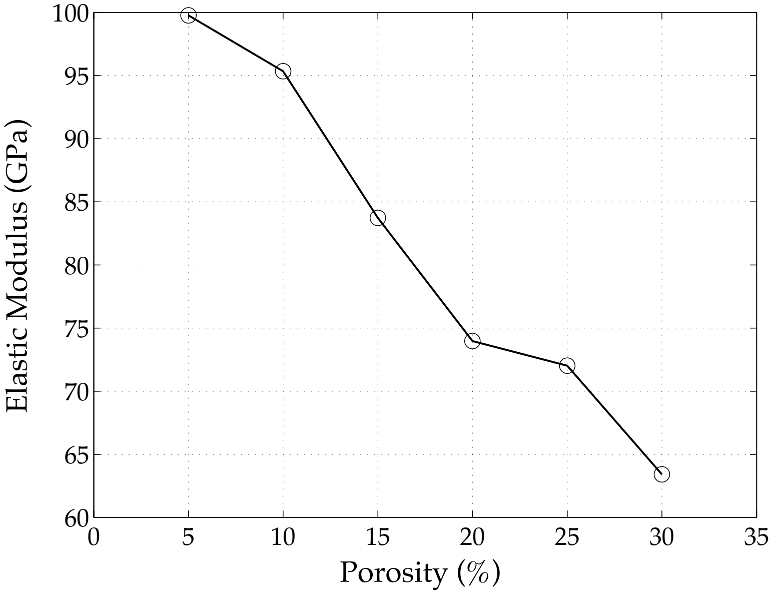

Figure 6.14: Plot showing the change in average elastic modulus (E) with increasing porosity

6.3 Comparison with Experimental Data

Having shown that the damage model could accurately mimic the physical characteristics of nanoindentation, the next step was to reveal whether those characteristics actually led to a realistic measure of the material itself. The simplest way to reach a conclusion was to simulate nanoindentation using similar parameters to those found in an experimental nanoindentation test, and observe whether material properties match up within some acceptable margin of error. Unfortunately, while material property data from experimental nanoindentation tests was readily available in literature, many of the testing parameters were omitted. For example, the porosity of the thermal barrier coating sample under examination was rarely reported. Without specific knowledge of the sample size, porosity and indenter dimensions, building an equivalent numerical simulation was impossible. Furthermore, the inherent differences in

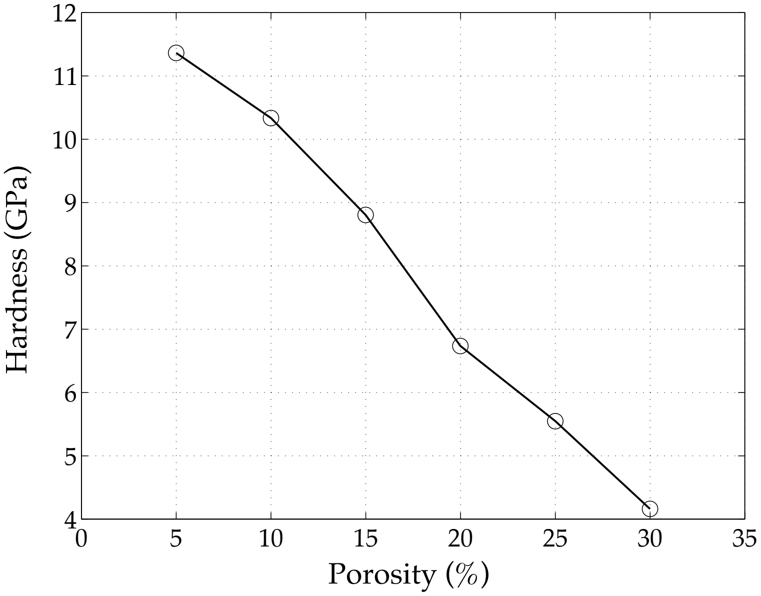

Figure 6.15: Plot showing the change in average hardness (H) with increasing porosity

microstructure geometry of every sample guaranteed that the prospect of matching material properties of a single experimental example was unrealistic.

To account for the aspects of the experimental data that could not be controlled, material properties measured by several authors were grouped together to establish a range of valid results for thermal barrier coatings. The properties generated by nanoindentation simulations could then be evaluated based on how well they fit within this range. Although this methodology did not confirm whether the damage model was able to recreate the exact outcome from any specific experimental test, it was still possible to validate the model's effectiveness with respect to the original design criterion: If the nanoindentation simulation could produce a range of material properties which fell within the acceptable bounds established from literature, it would suggest that the damage model was capable of serving as a numerical optimization tool to evaluate the performance of new microstructure designs.

For an initial comparison, Table 6.1 lists the range of material properties calculated by varying porosity in the nanoindentation simulation, along with several sets of experimental properties taken from literature. The experimental data is listed by author, with a range reported if multiple data points were provided. Comparing both the elastic modulus and hardness, the results found by the nanoindentation simulation conformed well with the experimental data, when taken as a whole. Some of the experimental data points extended beyond the predicted range, but differences in testing procedures and microstructure made this type of variability unavoidable.

Next, to inspect the correlation in elastic modulus, Figure 6.16 plots the values from

Table 6.1: Comparison of the material properties found in this study with experimental results taken from literature

References	**Properties**	
	Elastic Modulus (GPa)	Hardness (GPa)
This Study	62 - 100	4.1 - 11.4
Ghasemi (2013) [15]	106	5.87
Leigh (1997) [25]	33 - 106	2.69 - 6.34
Rico (2009) [39]	93	7.1
Shang (2013) [41]	104.13 - 149.63	3.97 - 10.39
Singh (1997) [42]	13.4 - 68.4	1.8 - 6.1
Thompson (2001) [47]	144.5	8.7
Wellman (2004) [51]	157	6.2
Zotov (2009) [53]	126	6.2

each author as a separate data set. The groups are arranged by the average of the points included in the set. The results produced by the nanoindentation simulation are colored in red. Each of the simulation data points corresponds to a different porosity, ranging from 5-30%, and is the average of multiple iterations of the same parameters to account for the random microstructure. Averages for the experimental and numerical data sets are plotted as horizontal lines.

The red points corresponding to the nanoindentation simulation fit directly in the center of the range of values for elastic modulus that were identified from literature. The clustering of the points is more precise than the experimental set, because they're averaged over many different potential microstructures. The correlation of the results can be evaluated using the averages plotted on Figure 6.16. The average modulus of the experimental set is only 18% greater than found by the simulation. This represents a good fit, considering the percent difference of highest value from the experimental data set to the lowest is 1072%.

Conducting the same analysis for the hardness, Figure 6.17 combines experimental and numerical values onto a single plot. Again, the results produced by the nanoindentation simulation are colored in red. Each of the simulation data points corresponds to a different porosity, and is the average of multiple iterations of the same parameters. Averages for the experimental and numerical data sets are plotted as horizontal lines.

Compared to Figure 6.16, the hardness values produced by the nanoindentation simulation do not exhibit the same precision. The simulation results span almost the same range as the experimental data, instead of fitting within the center of the range. Furthermore, the points representing lower amounts of porosity represent the two highest values of the entire

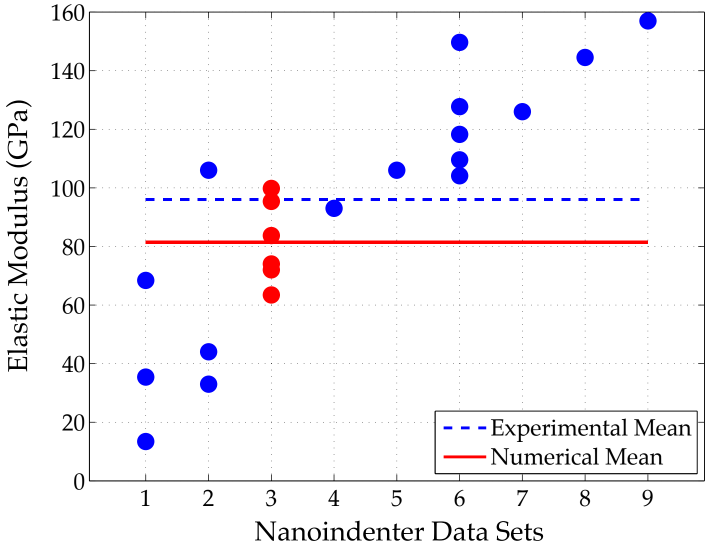

Figure 6.16: Range of values for elastic modulus (E) from experimental nanoindentation tests found in literature, each plotted as a separate data set. The red data set corresponds to values calculated from the simulation described in this work.

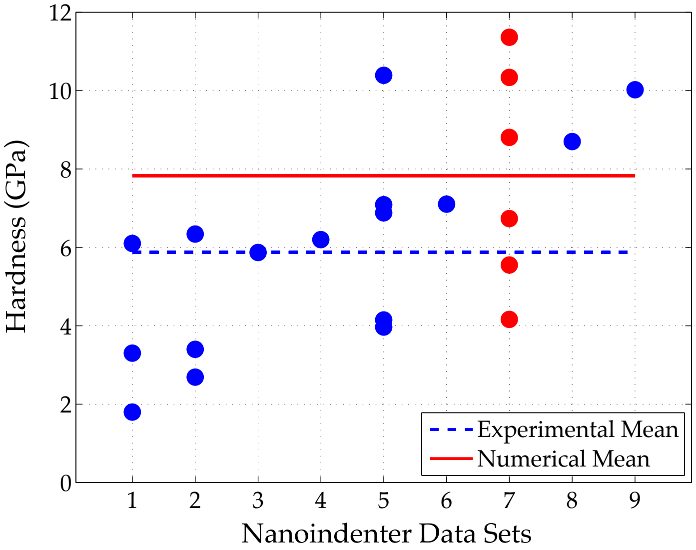

Figure 6.17: Range of values for hardness (H) from experimental nanoindentation tests found in literature, each plotted as a separate data set. The red data set corresponds to values calculated from the simulation described in this work.

set. The variance between averages is also greater, with the average experimental hardness lying 24.9% lower than found by the simulation. While still a good fit compared to the 477% spread in the range of experimental data, the above observations suggest that the damage model provides a slightly exaggerated amount of deformation resistance.

To explore this possibility further, Figure 6.18 graphs the same set of data with respect to both the elastic modulus and hardness. Keeping the two material properties coupled provides a more complete view of overall material performance, and thus, the damage model's ability to reproduce the relationship between the elastic modulus and hardness.

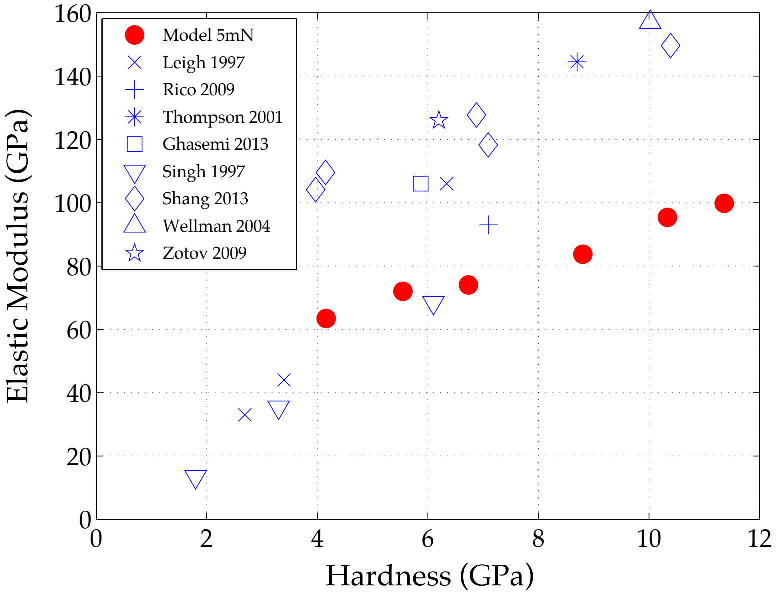

Figure 6.18: Plot comparing model results to experimental indentation data, showing the relationship between the elastic modulus and hardness

Despite the different testing conditions used by each author to produce the experimental data shown, a clear linear relationship between the elastic modulus and hardness can be seen. While the material properties generated by the damage model also exhibit a linear relationship, it has a lower gradient and does not follow the same path. Again, this suggests that the damage model was overestimating the material hardness to some extent.

6.3.1 Discussion of Overestimated Material Hardness

One potential explanation for inflated values of hardness observed in Figures 6.17 and 6.18 relates back to the method employed for microstructure assembly. Recalling Section 4.1.2, the microstructure details of the material were created by the random deletion of particles.

The intent was to reconstruct the pores and defects which exist between the yttria-stabilized zirconia splats produced by the air plasma spray process.

However, the random selection of pore location may not have provided a good enough approximation of an actual thermal barrier coating. Looking at the two images shown in Figure 6.19, a direct comparison can be made between the model's treatment of the microstructure and that of an actual thermal barrier coating [15].

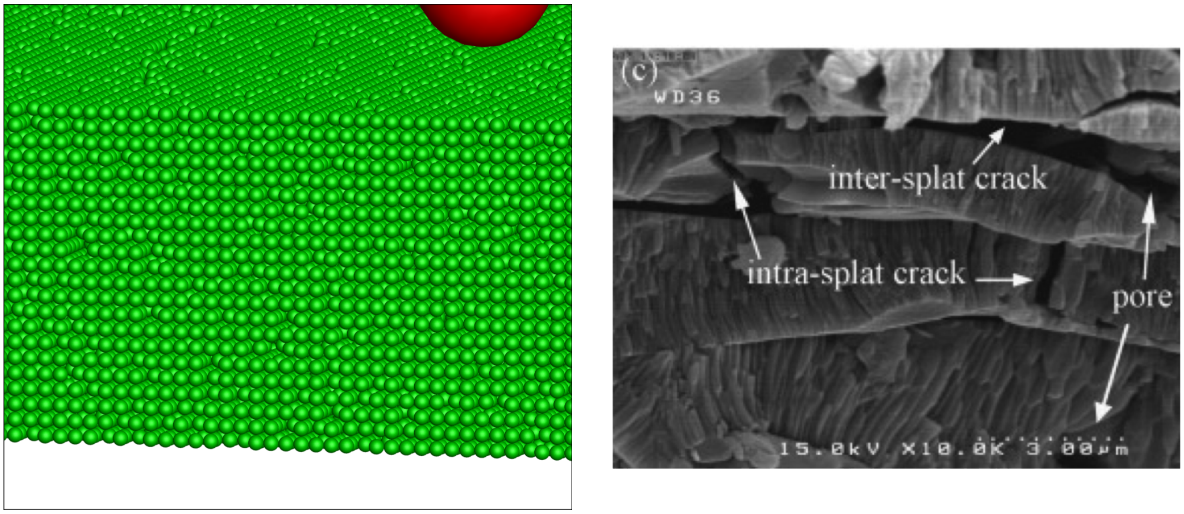

Figure 6.19: On the left, an example of a numerical microstructure generated by random deletion of particles. On the right is a contrasting image of an actual thermal barrier coating microstructure [15], which is characterized by weakly-connected splats. While the former is designed to be a recreation of the later, a visual comparison suggests that the attempt does not seem to be entirely successful.

Looking at the physical coating, the morphology is disconnected with pores and micro-cracks separating relatively homogeneous yttria-stabilized zirconia splats. Again, this is a result of the air plasma spray process. Molten droplets recrystallize on contact with the substrate, but form only weak connections with surrounding droplets that have already solidified. Those weak interfaces allow for significantly more deformation when subject to impact stresses than if the splats were fully bonded together.

The same description cannot be applied to the numerically defined microstructure in Figure 4.3. Although the amount of porosity was equivalent, randomly deleting particles allowed for a fully connected network of bonds to persist across the material domain. Thus, the "semi-crystalline" nature of the numerical microstructure may have provided an artificial increase in the material hardness, since the lack of weak interfaces made it more resistant to deformation. However, this imbalance can be rectified in future work by incorporating a more sophisticated method for particle assembly, which replicates the concept of weakly-connected splats.

Chapter 7

Conclusions

The goal of this research was to show that physical discrete element models have the potential to accurately simulate impact damage on a thermal barrier coating. This was demonstrated using multiple forms of validation, beginning with a basic simulation of impact damage by a foreign object. The observed sequence of damage corresponded with images of experimental impact tests. Characteristic impact damage phenomena, such as cratering and the formation of a large depression due to inelastic deformation, were present in the simulation. While not sufficient on its own, having the correct "look" can be a powerful form of confirmation in the field of computational mechanics.

The capabilities of the damage model were further validated by simulations of nanoindentation tests. The P-h curves generated by the simulation were a good match to the characteristic curves of thermal barrier coatings. Furthermore, the P-h curves showed instances of fracture damage and inelastic deformation that exactly matched experimental observations from literature. Most importantly, these damage modes were a natural consequence of the model behavior, strongly suggesting that it is accurately reproducing the physical processes that are caused by nanoindentation. When compared to the range of values for elastic modulus and hardness established by experimental data, the material properties exhibited by the damage model fit nearly in the center. Since the model values were averaged over dozens of different microstructure possibilities, matching the average of the reported numbers is the best possible outcome.

In conclusion, the damage model presented here has been demonstrated as a scientific tool to investigate the micro-mechanisms that combine to produce complex macroscopic behaviors in thermal barrier coatings. Eventually, the goal is to transform this model into an engineering tool to predict these macroscopic behaviors. While more work is certainly needed before the model can start to be used for "production-ready" design decisions, the results from this work have established that discrete element models can be used to accurately evaluate the performance and durability of porous ceramics, entirely through numerical methods.

7.1 Areas for Improvement

Although the results found from the damage model were quite promising, and matched well with experimental data, there is still ample room for improvement. The two aspects of the model that require the most reconsideration are both features chosen for sake of simplicity: the particle assembly pattern and the boundary conditions applied to the assembly. While the current methods did not significantly influence the outcome, a more careful treatment of both assumptions would lead to better accuracy and improved capabilities.

As mentioned in Section 4.1.2, any repeated pattern used to assemble particles will inevitably introduce anisotropy into the microstructure. While it wasn't a problem for this work, as all impact tests were conducted with an orientation of 90° with respect to the surface, it prevents the possibility of expanding the study to include angled impact trajectories. Since foreign objects undoubtedly strike from every conceivable direction, angled impact scenarios are a worthwhile area of study. Therefore, the capabilities of the model would be expanded by substituting a particle assembly algorithm that resulted in an isotropic microstructure. One potential method would be to imitate the air plasma spray process by shooting clusters of particles at random locations on a substrate. After the particles have dispersed following impact, bonds could be formed with near neighbors. This process could be repeated until an assembly of desired thickness was created. Since the placement of particles and bonds would be randomized by this process, the resulting assembly would lack any directional response to deformation.

Improvements can also be made to the boundary condition applied to the particle assembly. The current decision to use a rigid boundary was motivated by experimental impact testing, which utilize stationary fixtures to secure material samples. If not handled properly though, a rigid boundary can skew the results from the model by applying additional resistance. This effect was neglected in the model, with the reasoning that a sufficiently large domain will marginalize these types of edge effects. However, substituting a viscoelastic boundary condition instead would diminish the risk of edge effects even further. The artificial resistance would be reduced, potentially providing more accurate results. As an added benefit, a viscoelastic boundary condition would also provide additional damping of oscillations caused by impact and help the system reach equilibrium more quickly.

7.2 Future Applications

As a final note, the real potential for physical discrete element models becomes apparent when considering the possibility of direct microstructure design. Thermal barrier coatings are vulnerable to impact damage because current deposition technology cannot add a high volume fraction of porosity without sacrificing material strength. The two are unavoidably linked, as long as a coating is created by the random accumulation of droplets. However, the unfavorable coupling between thermal performance and durability could potentially be severed when material deposition can be controlled at a granular level. Once the technology exists to customize a microstructure, rapid design iteration powered by physically-accurate discrete element models will enable the creation of new classes of materials. Microstructure designs could be tuned for specific applications, identified entirely through numerical optimization. At the current rate of advancements in the areas of additive manufacturing and computational materials, it will not be long before these capabilities become a reality.

Bibliography

[1] Federal Aviation Administration. *Airplane Flying Handbook (FAA-H-8083-3A)*. Skyhorse Publishing Inc., 2011.

[2] J Alcal, A E Giannakopoulos, and S Suresh. “Continuous measurements of load-penetration curves with spherical microindenters and the estimation of mechanical properties”. In: *Journal of materials research* 13.5 (1998), pp. 1390–1400.

[3] Jorge Alcal. “Instrumented Microindentation of Zirconia Ceramics”. In: *Journal of the American Ceramic Society* 83.8 (2000), pp. 1977–1984.

[4] D Arbelaez, T I Zohdi, and D A Dornfeld. “Modeling and simulation of material removal with particulate flows”. In: *Computational Mechanics* 42.5 (2008), pp. 749–759.

[5] Sandip Basu, Alexander Moseson, and Michel W Barsoum. “On the determination of spherical nanoindentation stress-strain curves”. In: *Journal of materials research* 21.10 (2006), pp. 2628–2637.

[6] S I Bulychev et al. “Mechanical properties of materials studied from kinetic diagrams of load versus depth of impression during microimpression”. In: *Strength of Materials* 8.9 (1976), pp. 1084–1089.

[7] X Chen et al. “Foreign object damage in a thermal barrier system: mechanisms and simulations”. In: *Materials Science and Engineering a-Structural Materials Properties Microstructure and Processing* 352 (2003), pp. 221–231.

[8] Peter A Cundall and Otto DL Strack. “A discrete numerical model for granular assemblies”. In: *Geotechnique* 29.1 (1979), pp. 47–65.

[9] R M Davies. “The Determination of Static and Dynamic Yield Stresses Using a Steel Ball”. In: *Proceedings of the Royal Society A: Mathematical, Physical and Engineering Sciences* 197.1050 (June 1949), pp. 416–432.

[10] *ENGINEERING: PLASMA SPRAY PROCESS*. Mar. 2011. URL: `http://engg-learning.blogspot.com/2011/03/plasma-spray-process-inert-gas-such-as.html`.

[11] Anthony G Evans and R M Cannon. “Overview no. 48: Toughening of brittle solids by martensitic transformations”. In: *Acta metallurgica* 34.5 (1986), pp. 761–800.

[12] Anthony Glyn Evans et al. “Mechanisms controlling the durability of thermal barrier coatings”. In: *Progress in Materials Science* 46.5 (2001), pp. 505–553.

[13] Anthony C Fischer-Cripps. *Nanoindentation.* Springer, Aug. 2011.

[14] Y Gaillard, E Jimenez-Pique, and M Anglada. “Scale dependence of the Young’s modulus measured by nanoindentation in columnar YSZ EB-PVD thermal barriers coatings”. In: *Philosophical Magazine* 86.33-35 (2006), pp. 5441–5451.

[15] Reza Ghasemi et al. “Comparison of microstructure and mechanical properties of plasma-sprayed nanostructured and conventional yttria stabilized zirconia thermal barrier coatings”. In: *Ceramics International* (2013).

[16] John J Gilman. “Direct Measurements of the Surface Energies of Crystals”. In: *Journal of Applied Physics* 31.12 (1960), p. 2208.

[17] Takahiro Harada. *GPU Gems 3 - Chapter 29. Real-Time Rigid Body Simulation on GPUs.* URL: `http://http.developer.nvidia.com/GPUGems3/gpugems3_ch29.html`.

[18] Heinrich Hertz et al. *Miscellaneous Papers ... With an Introduction by ... P. Lenard. Authorised English Translation by D.E. Jones and G.A. Schott.* MacMillan and Co., Ltd. 1896.

[19] CEt Inglis. “Stresses in a plate due to the presence of cracks and sharp corners”. In: *SPIE MILESTONE SERIES MS* 137 (1997), pp. 3–17.

[20] Byung-Koog Jang and Hideaki Matsubara. “Hardness and Young’s modulus of nanoporous EB-PVD YSZ coatings by nanoindentation”. In: *Journal of Alloys and Compounds* 402.1-2 (Oct. 2005), pp. 237–241.

[21] K L Johnson and Kenneth Langstreth Johnson. *Contact mechanics.* Cambridge Univ Pr, Aug. 1987.

[22] H M KANDIL, J D GREINER, and J F SMITH. “Single-Crystal Elastic Constants of Yttria-Stabilized Zirconia in the Range 20 to 700C”. In: *Journal of the American Ceramic Society* 67.5 (May 1984), pp. 341–346.

[23] Anand Kulkarni et al. “Processing effects on porosity-property correlations in plasma sprayed yttria-stabilized zirconia coatings”. In: *Materials Science and Engineering: A* 359.1-2 (Oct. 2003), pp. 100–111.

[24] Brian R Lawn. *Fracture of brittle solids.* Cambridge Univ Pr, 1993.

[25] Sang Ha Leigh, Chung Kwei Lin, and Christopher C Berndt. “Elastic response of thermal spray deposits under indentation tests”. In: *Journal of the American Ceramic Society* 80.8 (1997), pp. 2093–2099.

[26] A E H Love. *A Treatise on the mathematical Theory of Elasticity.* Dover Pubns. 1944.

[27] J Malzbender and R.W. Steinbrech. “Determination of the stress-dependent stiffness of plasma-sprayed thermal barrier coatings using depth-sensitive indentation”. In: *Journal of materials research* 18.08 (2003), pp. 1975–1984.

[28] *Monthly Energy Review July 2012.* July 2012. URL: `http://www.eia.gov/totalenergy/data/monthly/archive/00351307.pdf`.

[29] R G Munro. "Analytical representations of elastic moduli data with simultaneous dependence on temperature and porosity". In: *JOURNAL OF RESEARCH-NATIONAL INSTITUTE OF STANDARDS AND TECHNOLOGY* 109.5 (2004), p. 497.

[30] Warren Carl Oliver and George Mathews Pharr. "Improved technique for determining hardness and elastic modulus using load and displacement sensing indentation experiments". In: *Journal of materials research* 7.6 (1992), pp. 1564–1583.

[31] E OROWAN. "Fracture and Strength of Solids". In: *Reports on Progress in Physics* 12 (1948), pp. 183–&.

[32] T M Pollock and S Tin. "Nickel-based superalloys for advanced turbine engines: Chemistry, microstructure, and properties". In: *Journal of Propulsion and Power* 22.2 (2006), pp. 361–374.

[33] Vitalii Postolenko. *Failure mechanisms of thermal barrier coatings for high temperature gas turbine components under cyclic thermal loading.* 2008.

[34] *Potential class — Pysic 0.4.8 documentation.* URL: `http://thynnine.github.io/pysic/potential%20class.html`.

[35] D O Potyondy and P A Cundall. "A bonded-particle model for rock". In: *International journal of rock mechanics and mining sciences* 41.8 (2004), pp. 1329–1364.

[36] A M Rajendran and J L Kroupa. "Impact damage model for ceramic materials". In: *Journal of Applied Physics* 66.8 (1989), p. 3560.

[37] N Ramakrishnan. "Effective elastic moduli of porous solids". In: *Journal of materials science* 25.9 (1990), pp. 3930–3937.

[38] Gerald W Recktenwald. *Numerical methods with MATLAB.* 2000.

[39] A Rico et al. "Mechanical properties of thermal barrier coatings after isothermal oxidation." In: *Surface and Coatings Technology* 203.16 (May 2009), pp. 2307–2314.

[40] H G Scott. "Phase relationships in the zirconia-yttria system". In: *Journal of materials science* 10.9 (1975), pp. 1527–1535.

[41] F Shang et al. "Determination of high-temperature mechanical properties of thermal barrier coatings by nanoindentation". In: (2013).

[42] J P Singh, M Sutaria, and M Ferber. "Use of Indentation Technique to Measure Elastic Modulus of Plasma-Sprayed Zirconia Thermal Barrier Coating". In: *onlinelibrary.wiley.com.* Hoboken, NJ, USA: John Wiley & Sons, Inc., Jan. 1997, pp. 191–200.

[43] R.W. Steinbrech. "Thermomechanical behavior of plasma sprayed thermal barrier coatings". In: *26th Annual Conference on Composites, Advanced Ceramics, Materials, and Structures: B: Ceramic Engineering and Science Proceedings* (2002), pp. 397–408.

[44] Ramesh Subramanian. “Impact on GT component coatings”. In: (Feb. 2011), pp. 1–13.

[45] *Superalloy - Wikipedia, the free encyclopedia.* URL: `http://en.wikipedia.org/wiki/Superalloy`.

[46] D Tabor. “A Simple Theory of Static and Dynamic Hardness”. In: *Proceedings of the Royal Society A: Mathematical, Physical and Engineering Sciences* 192.1029 (Feb. 1948), pp. 247–274.

[47] J A Thompson and T W Clyne. “The effect of heat treatment on the stiffness of zirconia top coats in plasma-sprayed TBCs”. In: *Acta Materialia* 49.9 (May 2001), pp. 1565–1575.

[48] Stephen Timoshenko and J N Goodier. *Theory of Elasticity.* McGraw-Hill book Company. 1951.

[49] A. Tsoga and P. Nikolopoulos. “Surface and grain-boundary energies in yttria-stabilized zirconia (YSZ-8 mol)”. In: *Journal of materials science* 31.20 (1996), pp. 5409–5413.

[50] Darren P Unger and Howard J Herzog. *Comparative Study on Energy R&D Performance: Gas Turbine Case Study.* Energy Laboratory, Massachusetts Institute of Technology, Aug. 1998.

[51] R G Wellman, A Dyer, and J R Nicholls. “Nano and micro indentation studies of bulk zirconia and EB PVD TBCs”. In: *Surface and Coatings Technology* 176.2 (2004), pp. 253–260.

[52] Jackson C S Yang and Do Sup Chun. *Application of the Hertz Contact Law to Problems of Impact in Plates.* 1969.

[53] N Zotov, M Bartsch, and G Eggeler. “Thermal barrier coating systems — analysis of nanoindentation curves”. In: *Surface and Coatings Technology* 203.14 (Apr. 2009), pp. 2064–2072.